



Computer Aided Diagnosis system for prostatic biopsy guidance and follow-up fusing multi-modal imaging.

Guillaume Lemaître

LE2I - ViCOROB

Université de Bourgogne - Universitat de Girona

Supervisors:

Jordi Freixenet Bosch (ViCOROB - UdG)

Fabrice Mériaudeau (CISIR - UTP)

Robert Marí Marly (ViCOROB - UdG)

Paul Michael Walker (LE2I - UBFC)

A thesis submitted for the degree of

Philosophiæ Doctor (PhD)

April 2015

1. Reviewer: Name

2. Reviewer:

Day of the defense:

Signature from head of PhD committee:

Abstract

Put your abstract or summary here, if your university requires it.

To ...

Acknowledgements

I would like to acknowledge the thousands of individuals who have coded for the LaTeX project for free. It is due to their efforts that we can generate professionally typeset PDFs now.

Contents

List of Abbreviations	v
List of Figures	ix
List of Tables	xi
1 Introduction	1
1.1 Prostate anatomy	1
1.2 Prostate carcinoma	2
1.3 prostate cancer (CaP) screening and imaging techniques	3
1.4 Computer-aided systems for CaP	5
1.5 Research motivation	6
1.6 Thesis outline	6
2 MRI Principles and Imaging Techniques	7
2.1 MRI principles	7
2.2 MRI imaging techniques	7
2.2.1 T ₂ -W MRI	9
2.2.2 T ₂ map	9
2.2.3 DCE magnetic resonance imaging (MRI)	11
2.2.4 DW MRI	14
2.2.5 ADC Map	16
2.2.6 MRSI	17
3 Review of CADe and CADx for CaP	21
3.1 Image regularization framework	24
3.1.1 Pre-processing	24

CONTENTS

3.1.2	Segmentation	34
3.1.3	Registration	38
3.2	Image classification framework	43
3.2.1	Computer-aided detection (CAdE): region of interests (ROIs) de- tection/selection	43
3.2.2	Computer-aided diagnosis (CAdx): Feature detection	44
3.2.2.1	Image-based features	44
3.2.2.2	Dynamic contrast-enhanced (DCE)-based features	48
3.2.2.3	Magnetic resonance spectroscopy imaging (MRSI)-based features	51
3.2.3	CAdx: Feature selection and feature extraction	52
	References	53

List of Abbreviations

ACM	active contour model
ADC	apparent diffusion coefficient
AIF	arterial input function
ASM	active shape model
BPH	benign prostatic hyperplasia
CAD	computer-aided detection and diagnosis
CADe	computer-aided detection
CADx	computer-aided diagnosis
CaP	prostate cancer
CG	central gland
Chap.	Chapter
CMI	combined mutual information
CSE	chemical shift effect
CZ	central zone
DCE	dynamic contrast-enhanced
DCT	discrete cosine transform
DFT	discrete fourier transform
DW	diffusion weighted
EES	extravascular-extracellular space
Eq.	equation
ERSSPC	European Randomized Study of Screening for Prostate Cancer

CONTENTS

ES Evolution Strategy

Fig. figure

FOV field of view

FSE Fast Spin-Echo

GS Gleason score

***g*-scale** generalized scale

HOG histogram of oriented gradient

ITK Insight Segmentation and Registration Toolkit

***k*-NN** *k*-nearest neighbour

LBP local binary pattern

LDA linear discriminant analysis

MANTRA multi-attribute non-initializing texture reconstruction based active shape model

MAP maximum *a posteriori*

MI mutual information

MRI magnetic resonance imaging

MRSI magnetic resonance spectroscopy imaging

MSE mean squared error

NMR nuclear magnetic resonance

PCA principal components analysis

PDF probability density function

PLCO Prostate Lung Colorectal and Ovarian

PSA prostate-specific antigen

PZ peripheral zone

RBF radial basis function

ROI region of interest

Sect. section

SI signal intensity

SNR signal-to-noise

STAPLE simultaneous truth and performance level estimation

SVD singular value decomposition

SVM support vector machines

T₁-W T₁ Weighted

T₂-W T₂ Weighted

TE echo time

TPS thin plate spline

TR repetition time

TRUS transrectal ultrasound

TZ transitional zone

US ultrasound

WERITAS weighted ensemble of regional image textures for active shape model segmentation

CONTENTS

List of Figures

1.1	Sagittal anatomy of prostate.	1
1.2	Prostate anatomy.	2
2.1	computer-aided detection and diagnosis (CAD) framework using multi-parametric MRI images.	10
2.2	Rendering of T ₂ Weighted (T ₂ -W)-MRI prostate images.	11
2.3	Enhancement of DCE-MRI signal.	12
2.4	Example of diffusion weighted (DW)-MRI and DCE map.	14
2.5	Illustration of healthy and cancerous MRSI spectrum.	17
3.1	Illustration of a Gaussian and Rayleigh distributions.	24
3.2	Inhomogeneity artefacts due to perturbation of the endorectal coil.	26
3.3	Example of linear mapping by parts as proposed by (1).	30
3.4	Illustration of the two organs used by (2, 3) to normalize T ₂ -W and T ₁ Weighted (T ₁ -W) MRI images.	31
3.5	Illustration of phase malignant in an MRSI spectra.	31
3.6	Illustration of water and fat residues in MRSI signal after supression during acquisition.	32
3.7	Illustration of frequency misalignment in an MRSI spectra.	34
3.8	Regsitration framework.	38
3.9	Difference observed in joint histogram between aligned and misaligned images.	40
3.10	Illustration of four different Gabor filters.	45
3.11	Semi-quantitative features used for DCE-MRI.	50

LIST OF FIGURES

List of Tables

2.1	Overview of the features associated with each MRI modality used for medical diagnosis by radiologists. Acronyms: prostate cancer (CaP) - signal intensity (SI) - Gleason score (GS).	8
3.1	Overview of the different studies reviewed with their main characteristics. Acronyms: number (#) - image regularization (Img. Reg.).	23
3.2	Overview of the pre-processing methods used in CAD systems.	35
3.3	Overview of the segmentation methods used in CAD systems.	35
3.4	Classification of the different registration methods used in the CAD systems reviewed. Acronyms: gradient descent (GD), Nelder-Mead (NM). . .	42
3.5	Overview of the CADe strategies employed in CAD systems.	43
3.6	The fourteen statistical features for texture analysis commonly computed from the gray level co-occurrence matrix p as presented by (4).	46
3.7	Parameters used as features for a DCE semi-quantitative analysis in CAD systems.	49

LIST OF TABLES

Chapter 1

Introduction

1.1 Prostate anatomy

The prostate is an exocrine gland of the male reproductive system having an inverted pyramidal shape, which is located below the bladder and in front of the rectum (see Fig. 1.1). It measures approximately three centimetres in height by two and half centimetres in depth and its weight is estimated to be between seven and sixteen grams for an adult (6). The prostate size increases at two distinct stages during physical development: initially at puberty to reach its normal size, then again after sixty years of age leading to benign prostatic hyperplasia (BPH) (7).

A zonal classification of the prostate, depicted in Fig. 1.2, was suggested by McNeal (8). Subsequently, this categorization was widely accepted in the literature (cf., (7,

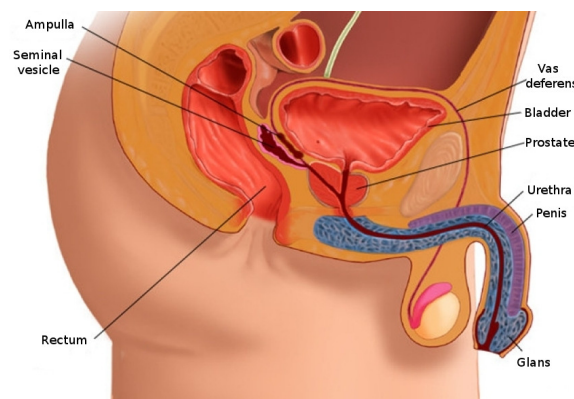
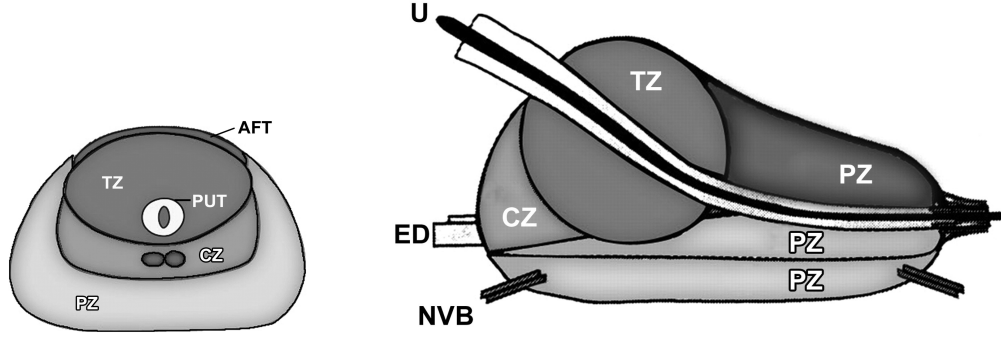


Figure 1.1: Sagittal anatomy scheme of the male reproductive system.

1. INTRODUCTION



(a) Transverse anatomy of the prostate.

(b) Sagittal anatomy of the prostate.

Figure 1.2: Prostate anatomy with division in different zones. *AFT*: anterior fibromuscular tissue, *CZ*: central zone, *ED*: ejaculatory duct, *NVB*: neurovascular bundle, *PUT*: tissue, *PZ*: peripheral zone, *U*: urethra, *TZ*: transitional zone, *B*: base, *M*: median, *A*: apex (copyright by (5)).

9, 10, 11)) and is used in all medical examinations (e.g., biopsy, MRI screening. The classification is based on dividing the gland into three distinct regions: (i) central zone (CZ) accounting for 20-25% of the whole prostate gland, (ii) transitional zone (TZ) standing for 5% and (iii) peripheral zone (PZ) representing the 70%. In MRI images, tissues of CZ and TZ are difficult to distinguish and are usually merged into a common region, denominated central gland (CG). As part of this classification, the prostate can be divided in three longitudinal portions depicted in Fig. 1.2(b): (i) base, (ii) median gland and (iii) apex.

1.2 Prostate carcinoma

Prostate cancer (CaP) has been reported on a worldwide scale to be the second most frequently diagnosed cancer of men accounting for 13.6% (12). Statistically, in 2008, the number of new diagnosed cases was estimated to be 899,000 with no less than 258,100 deaths (12). In United States, aside from skin cancer, CaP was declared to be the most commonly diagnosed cancer among men, implying that approximately one in six men will be diagnosed with CaP during their lifetime and one in thirty-six will die from this disease causing CaP to be the second most common cause of cancer death among men

(13), (14).

Despite active research to determine the causes of prostate cancer, a fuzzy list of risk factors has arisen (15). The etiology was linked to the following factors (15): (i) family history (16, 17), (ii) genetic factors (18, 19, 20), (iii) race-ethnicity (16, 21), (iv) diet (16, 22, 23), and (v) obesity (16, 24). This list of risk factors alone cannot be used to diagnose CaP and in this way, screening enables early detection and treatment.

CaP growth is characterized by two main types of evolution (25): slow-growing tumours, accounting for up to 85 % of all CaPs (26), progress slowly and usually stay confined to the prostate gland. For such cases, treatment can be substituted with active surveillance. In contrast, the second variant of CaPs develops rapidly and metastasises from prostate gland to others organs, primarily the bones (27). Bone metastases, being an incurable disease, significantly affects the morbidity and mortality rate (28). Hence, the results of the surveillance have to be trustworthy in order to distinguish aggressive from slow-growing CaP.

CaP is more likely to come into being in specific regions of the prostate. In that respect, around 70-80 % of CaPs originate in PZ whereas 10-20 % in TZ (29, 30, 31). Only about 5 % of CaPs occur in CZ (30, 32). However, those cancers appear to be more aggressive and more likely to invade other organs due to their location (32).

1.3 CaP screening and imaging techniques

Current CaP screening consists of three different stages. First, prostate-specific antigen (PSA) control is performed to distinguish between low and high risk CaP. Then, for confirmation, samples are taken during prostate biopsy and finally analysed to evaluate the prognosis and the stage of CaP. In this section, we present a detailed description of the current screening as well as its drawbacks.

Since its introduction in mid-1980s, PSA is widely used for CaP screening (33). A higher-than-normal level of PSA can indicate an abnormality of the prostate either as a BPH or a cancer (34). However, other factors can lead to an increased PSA level such as prostate infections, irritations, a recent ejaculation or a recent rectal examination (7). PSA can be found in the bloodstream in two different forms: free PSA (about 10%), and linked to another protein (about 90%). A level of PSA higher than 10 ng.mL^{-1} is considered to be at risk (7). If the PSA level is between 10 ng.mL^{-1} and 4 ng.mL^{-1} ,

1. INTRODUCTION

the patient is considered as suspicious (35). In that case, the ratio of free PSA to total PSA is computed; if the ratio is higher than 15%, the case is considered as pathological (7).

A transrectal ultrasound (TRUS) biopsy is carried out for cases which are considered as pathological. At least six different samples are taken randomly from the right and left parts of three different zones: apex, median and base. These samples are further evaluated using the Gleason grading system (36). The scoring scheme to characterize the biopsy sample is composed of five different patterns which correspond to grades ranging from 1 to 5. Higher grades are associated with poor prognosis (37). Then, in the Gleason system, two scores are assigned corresponding to (i) the grade of the most present tumour pattern, and (ii) the grade of the second most present tumour pattern (37). A higher GS indicates a more aggressive tumour (37). Also, it should be noted that biopsy is an invasive procedure which can result in serious infection or urine retention (38, 39).

Although PSA screening has been shown to improve early detection of CaP (39), its lack of reliability motivates further investigations using MRI-CAD. Two reliable studies, carried out in the United States (40) and in Europe (41, 42), have attempted to assess the impact of early detection of CaP, with diverging outcomes (39, 43). The study carried out in Europe¹ concluded that PSA screening reduces CaP-related mortality by 21-44% (41, 42), while the American² trial found no such effect (40). However, both studies agree that PSA screening suffers from low specificity, with an estimated rate of 36 % (44). Both studies also agree that over-treatment is an issue: decision making regarding treatment is further complicated by difficulties in evaluating the aggressiveness and progression of CaP (45).

Hence, new screening methods should be developed with improved specificity of detection as well as more accurate risk assessment (aggressiveness and progression). Current research is focused on identifying new biological markers to replace PSA-based screening (46, 47, 48). Until such research comes to fruition, these needs can be met through active-surveillance strategy using multi-parametric MRI techniques (34, 49).

¹The European Randomized Study of Screening for Prostate Cancer (ERSSPC) started in the 1990s in order to evaluate the effect of PSA screening on mortality rate.

²The Prostate Lung Colorectal and Ovarian (PLCO) cancer screening trial is carried out in the United States and intends to ascertain the effects of screening on mortality rate.

An MRI-CAD system, which is an area of active research and forms the focus of this thesis, can be incorporated into this screening strategy allowing a more systematic and rigorous follow-up.

Another weakness of the current screening strategy lies in the fact that TRUS biopsy does not provide trustworthy results. Due to its “blind” nature, there is a chance of missing aggressive tumours or detecting microfocal “cancers”, which influences the aggressiveness-assessment procedure (50). As a consequence, over-diagnosis is estimated at up to 30 % (51), while missing clinically significant CaP is estimated at up to 35 % (52). In an effort to solve both issues, alternative biopsy approaches have been explored. MRI/ultrasound (US)-guided biopsy has been shown to outperform standard TRUS biopsy (53). There, multimodal MRI images are fused with US images in order to improve localization and aggressiveness assessment to carry out biopsies. Human interaction plays a major role in biopsy sampling which can lead to low repeatability; by reducing potential human errors at this stage, the CAD framework can be used to improve repeatability of examination. CaP detection and diagnosis benefit from the use of CAD and MRI techniques.

In an effort to improve the current state of CaP diagnosis and detection, this thesis is intended to provide a multiparametric MRI CAD system. MRI principles and its different modalities are presented in Chapter (Chap.) 2.

1.4 Computer-aided systems for CaP

During the last century, physicists have focused on constantly innovating in terms of imaging techniques assisting radiologists to improve cancer detection and diagnosis. However, human diagnosis still suffers from low repeatability, synonymous with erroneous detection or interpretations of abnormalities throughout clinical decisions (54, 55). These errors are driven by two major causes (54): observer limitations (e.g., constrained human visual perception, fatigue or distraction) and the complexity of the clinical cases themselves, for instance due to unbalanced data (number of healthy cases more abundant than malignant cases) or overlapping structures.

Computer vision has given rise to many promising solutions, but, instead of focusing on fully automatic computerized systems, researchers have aimed at providing computer image analysis techniques to aid radiologists in their clinical decisions (54). In fact,

1. INTRODUCTION

these investigations brought about both concepts of CAdE and CAdx grouped under the acronym CAD. Since those first steps, evidence has shown that CAD systems enhance the diagnosis performance of radiologists. Chan *et al.* reported a significant 4 % improvement in breast cancer detection (56), which has been confirmed in later studies (57). Similar conclusions were drawn in the case of lung nodule detection (58), colon cancer (59) and CaP as well (55). Chan *et al.* (56) also hypothesized that CAD systems will be even more efficient assisting inexperienced radiologists than senior radiologists. That hypothesis was tested by Hambrock *et al.* (55) and was confirmed in case of CaP detection. In this particular study, inexperienced radiologists obtained equivalent performance to senior radiologists, both using CAD whereas the accuracy of their diagnosis was significantly poorer without CAD's help.

In contradiction with the aforementioned statement, CAD for CaP is a young technology due to the fact that is based on MRI (60). Four distinct MRI modalities are employed in CaP diagnosis which were mainly developed after the mid-1990s: (i) T₂-W MRI (61), (ii) DCE MRI (62), (iii) MRSI (63) and (iv) DW MRI (64). In addition, the increase of magnetic field strength (from 1.5 to 3 Tesla) and the development of endorectal coils, both improved image spatial resolution (65) needed to perform more accurate diagnosis. It is for this matter that the development of CAD for CaP is still lagging behind fields stated above.

This research is aimed at first, to provide an overview of the current state-of-the-art of CAD for CaP and later, according to the drawn conclusions, to propose a CAD which takes advantage of multiparametric MRI modalities. A review of the current proposed CAD for CaP is presented in Chap. 3.

1.5 Research motivation

1.6 Thesis outline

Chapter 2

MRI Principles and Imaging Techniques

2.1 MRI principles

2.2 MRI imaging techniques

MRI provides promising imaging techniques to overcome the previous mentioned drawbacks. Unlike TRUS biopsy, MRI examination is a non-invasive protocol and has been shown to be the most acute and harmless technique available currently (66). In this section, we review different MRI techniques developed for CaP detection and diagnosis. Features strengthening each modality, will receive particular attention together with their drawbacks. Commonly, these features form the basis for developing analytic tools and automatic algorithms. However, we refer the reader to Sect.. ?? for more details on automatic feature detection methods since they are part and parcel of the CAD framework. Table 2.1 provides an overview of the following discussion.

Table 2.1: Overview of the features associated with each MRI modality used for medical diagnosis by radiologists. Acronyms: prostate cancer (CaP) - signal intensity (SI) - Gleason score (GS).

Modality	Significant features	CaP	Healthy tissue	GS correlation
T ₂ -W MRI	SI Shape	low-SI in PZ (9) round or ill-defined mass in PZ (61)	intermediate to high-SI in PZ (9)	+ (67)
	SI Shape	low-SI in CG (35, 68) homogeneous mass with ill-defined edges in CG (35, 68)	low-SI in CG (35, 68)	
T ₂ map	SI	low-SI (69, 70)	intermediate to high-SI (69, 70)	+ (69, 71, 72)
DCE MRI	Semi-quantitative features (73): – wash-in – wash-out – integral under the curve – maximum signal intensity – time-to-peak enhancement	faster faster higher higher faster	slower slower lower lower slower	0 0 0 0 0
	Quantitative features (Tofts' parameters (74)): – k_{ep} – K^{trans}	higher higher	lower lower	0 0
DW MRI	SI	higher-SI (35, 75)	lower-SI (35, 75)	+
ADC map	SI	low-SI (35)	high-SI (35)	+ (76, 77, 78)
MRSI	Metabolites:			
	Citrate (2.64 ppm) (79)	lower concentration (80, 81, 82)	higher concentration (80, 81, 82)	+ (83)
	Choline (3.21 ppm) (79)	higher concentration (80, 81, 82)	lower concentration (80, 81, 82)	0 (83)
	Spermine (3.11 ppm) (79)	lower concentration (80, 81, 82)	higher concentration (80, 81, 82)	+ (83)

Notes:

+ = significantly correlated.

0 = no correlation.

2.2.1 T_2 -W MRI

T_2 -W MRI was the first MRI-modality used to perform CaP diagnosis using MRI (61). Nowadays, radiologists make use of it for CaP detection, localization and staging purposes. This imaging technique is well suited to render zonal anatomy of the prostate (35).

This modality relies on a sequence based on setting a long repetition time (TR), reducing the T_1 effect in nuclear magnetic resonance (NMR) signal measured, and fixing the echo time (TE) to sufficiently large values in order to enhance the T_2 effect of tissues. Thus, PZ and CG tissues are well perceptible in these images. The former is characterized by an intermediate/high-SI while the latter is depicted by a low-SI (9). An example of a healthy prostate is shown in Fig. 2.2(a).

In PZ, round or ill-defined low-SI masses are synonymous with CaPs (61) as shown in Fig. 2.2(b). Detecting CaP in CG is more challenging. In fact both normal CG tissue and malignant tissue, have a low-SI in T_2 -W MRI reinforcing difficulties to distinguish between them. However, CaPs in CG appear often as homogeneous mass possessing ill-defined edges with lenticular or “water-drop” shapes (35, 68) as depicted in Fig. 2.2(c).

CaP aggressiveness was shown to be inversely correlated with SI. Indeed, CaPs assessed with a GS of 4-5 implied lower SI than the one with a GS of 2-3 (67).

In spite of the availability of these useful and encouraging features, the T_2 -W modality lacks reliability (34, 84). Sensitivity is affected by the difficulties in detecting cancers in CG (84) while specificity rate is highly affected by outliers (35). In fact, various conditions emulate patterns of CaP such as BPH, post-biopsy haemorrhage, atrophy, scars and post-treatment (9, 35, 64, 85, 86). These issues can be partly addressed using more innovative and advanced modalities.

2.2.2 T_2 map

As previously mentioned, T_2 -W MRI modality shows low sensitivity. Moreover, T_2 -W MRI images are a composite of multiple effects (60). However, T_2 values alone have been shown to be more discriminative (71) and highly correlated with citrate concentration, a biological marker in CaP (69, 72).

2. MRI PRINCIPLES AND IMAGING TECHNIQUES

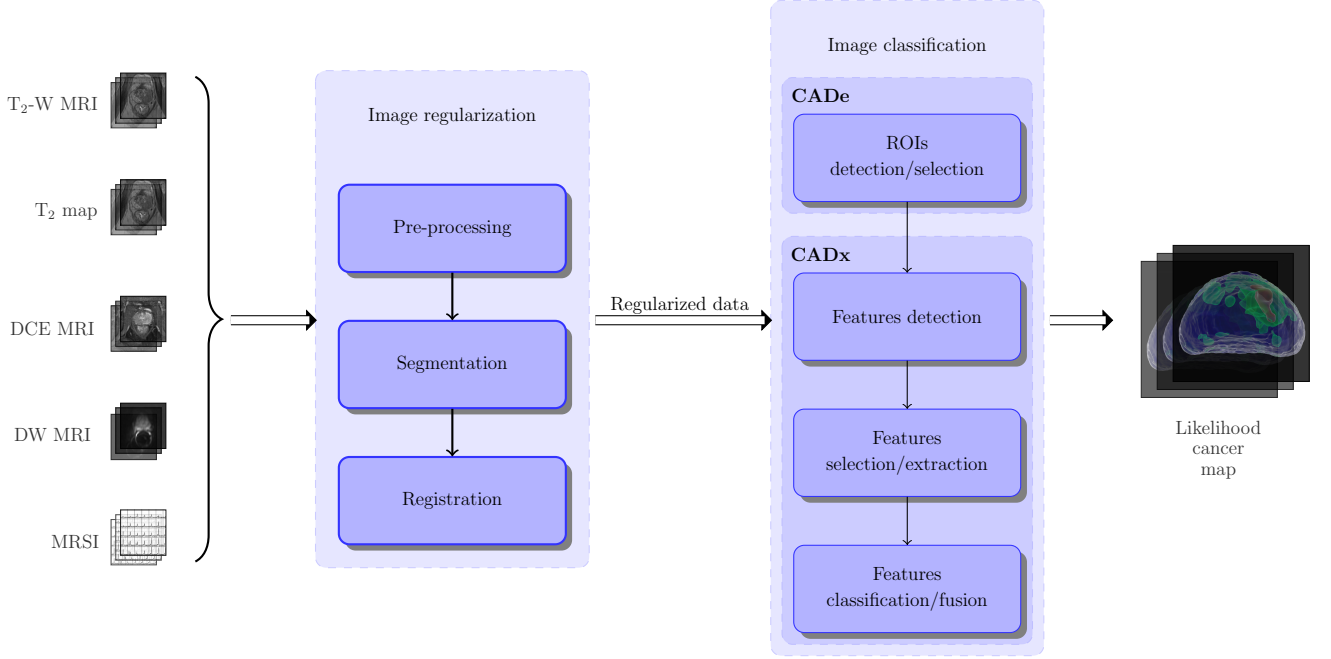
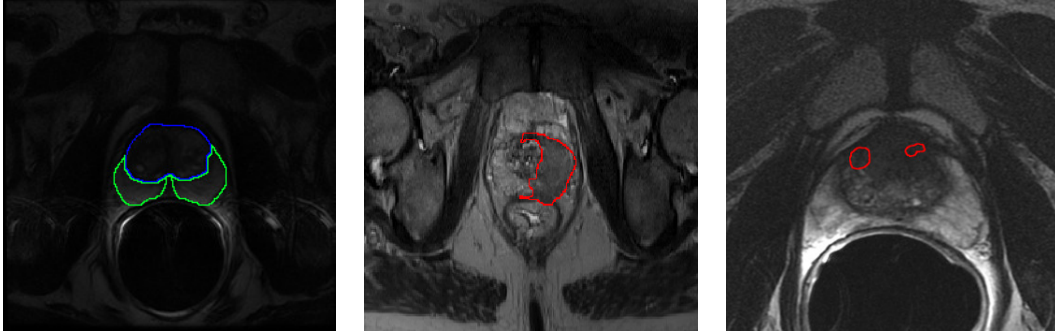


Figure 2.1: CAD framework using MRI images. Multiparametric MRI images are provided as inputs. These data arise from heterogeneous sources and need to be regularized. Some studies do not consider this stage as mandatory and do not implement or only partly those processes (see Tab. 3.1). A pre-processing stage is usually applied to standardize the intensity of images, reduce noise and artefacts. Then, in the image set, the prostate organ has to be segmented to focus the next processing stages only on that particular ROI. Moreover, prostate location can vary depending of the modality chosen. Therefore, the images are registered so that all segmented images will be in the same reference frame. Once the image regularisation performed, image classification can be carried out. First, a strategy defining ROIs to focus on is decided. Then, distinctive features are extracted before to be post-processed to select the most salient features. Finally, these salient features will feed a classifier previously trained which will provide a likelihood cancer map associated with either CaP detection or diagnosis.



(a) T₂-W-MRI slice of an healthy prostate acquire with a 1.5 Tesla MRI. The blue contour represents the CG while the PZ corresponds to the green contour.

(b) T₂-W-MRI slice of a prostate with a CaP highlighted in the PZ using a 3.0 Tesla MRI scanner.

(c) T₂-W-MRI slice of a prostate with a CaP highlighted in the CG using a 3.0 Tesla MRI scanner.

Figure 2.2: Rendering of T₂-W-MRI prostate image with both 1.5 and 3.0 Tesla MRI scanner.

T₂ values are computed using the characteristics of transverse relaxation which is formalized as:

$$M_{x,y}(t) = M_{x,y}(0) \exp\left(-\frac{t}{T_2}\right), \quad (2.1)$$

where $M_{x,y}(0)$ is the initial value of $M_{x,y}(t)$ and T_2 is the relaxation time. By rearranging Eq. 2.1, T₂ map is computed performing a linear fitting on the model in Eq. 2.2 using several TE, $t = \{TE_1, TE_2, \dots, TE_m\}$.

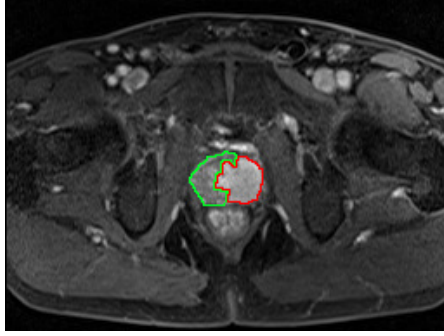
$$\ln\left[\frac{M_{x,y}(t)}{M_{x,y}(0)}\right] = -\frac{t}{T_2}. \quad (2.2)$$

The Fast Spin-Echo (FSE) sequence has been shown to be particularly well suited in order to build a T₂ map and obtain accurate T₂ values (87). Similar to T₂-W MRI, T₂ values associated with CaP are significantly lower than those of healthy tissues (69, 70).

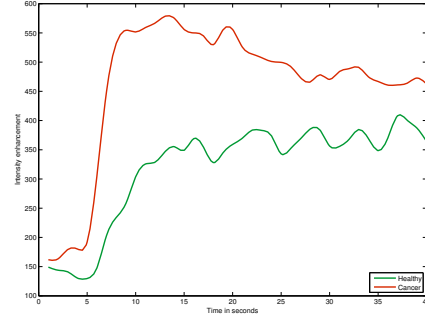
2.2.3 DCE MRI

DCE MRI is an imaging technique which exploits the vascularity characteristic of tissues. Contrast media, usually gadolinium-based, is injected intravenously into the patient. The media extravasates from vessels to extravascular-extracellular space (EES)

2. MRI PRINCIPLES AND IMAGING TECHNIQUES



(a) T_1 -W-MRI image where the cancer is delimited by the red contour. The green area was still not invaded by the CaP



(b) Enhancement curve computed during the DCE-MRI analysis. The red curve is typical from CaP cancer while the green curve is characteristic of healthy tissue.

Figure 2.3: Illustration of typical enhancement signal observed in DCE-MRI analysis collected with a 3.0 Tesla MRI scanner.

and is released back into the vasculature before being eliminated by the kidneys (88). Furthermore, the diffusion speed of the contrast agent may vary due to several parameters: (i) the permeability of the micro-vessels, (ii) their surface area and (iii) the blood flow (89).

Healthy PZ is mainly made up of glandular tissue, around 70 % (5), which implies a reduced interstitial space restricting exchanges between vessels and EES (90, 91). Normal CG has a more disorganised structure, composed of mainly fibrous tissue (5, 34), which facilitates the arrival of the contrast agent in EES (92). To understand the difference between contrast media kinetic in malignant tumours and the two previous behaviours mentioned, one has to focus on the process known as angiogenesis (93). In order to ensure growth, malignant tumours produce and release angiogenic promoter substances (93). These molecules stimulate the creation of new vessels towards the tumour (93). However, the new vessel networks in tumours differ from those present in healthy tissue (88). They are more porous due to the fact that their capillary walls have a large number of “openings” (5, 88). In contrast to healthy cases, this increased vascular permeability results in increased contrast agent exchanges between vessels and EES (73).

By making use of the previous aspects, DCE MRI is based on an acquisition of a set of T_1 -W MRI images over time. The Gadolinium-based contrast agent shortens T_1

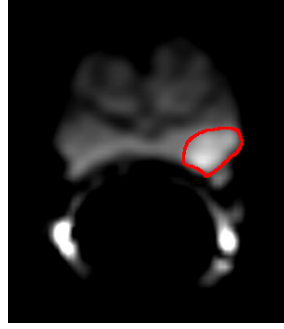
relaxation time enhancing contrast in T_1 -W MRI images. The aim is to post-analyse the pharmacokinetic behaviour of the contrast media concentration in prostate tissues (73). The image analysis is carried out in two dimensions: (i) in the spatial domain on a pixel-by-pixel basis and (ii) in the time domain corresponding to the consecutive images acquired with the MRI. Thus, for each spatial location, a signal linked to contrast media concentration is measured as shown in Fig. 2.3(b) (74).

By taking the previous remarks regarding medical aspects and signal theory into account, CaPs are characterized by a signal having an earlier and faster enhancement and an earlier wash-out (cf., the rate of the contrast agent flowing out of the tissue) (see Fig. 2.3(b)) (73). Three different approaches exist to analyse these signals with the aim of tagging them as corresponding to either normal or malignant tissues. Qualitative analysis is based on assessment of the signal shape (34).

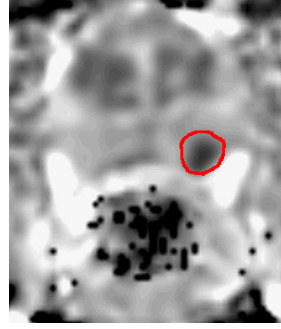
Quantitative approaches consist of inferring pharmacokinetic parameter values (74). Those parameters are part of mathematical-pharmacokinetic models which are directly based on physiological exchanges between vessels and EES. Several pharmacokinetic models were proposed such as the Kety model (94), the Tofts model (95) and mixed models (96, 97). The last family of methods mixed both approaches and are grouped together under the heading of semi-quantitative methods. They rely on shape characterization using mathematical modelling to extract a set of parameters such as wash-in gradient, wash-out, integral under the curve, maximum signal intensity, time-to-peak enhancement and start of enhancement. These parameters will be discussed in a later section (see Fig. 3.11) (34, 73). It was shown that semi-quantitative and quantitative methods improve localization of CaP when compared with qualitative methods (98). Section ?? provides a full description of quantitative and semi-quantitative approaches.

DCE MRI combined with T_2 -W MRI has shown to enhance sensitivity compared to T_2 -W MRI alone (99, 100, 101, 102). Despite this fact, DCE MRI possesses some drawbacks. Due to its “dynamic” nature, patient motions during the image acquisition lead to spatial misregistration of the image set (73)). Furthermore, it has been suggested that malignant tumours are difficult to distinguish from prostatitis located in PZ and BPH located in CG (34, 73). These pairs of tissues tend to have similar appearances. Later studies have shown that CaPs in CG do not always manifest in homogeneous fashion. Indeed, tumours in this zone can present both hypo-vascularization and hyper-vascularization which illustrates the challenge of CaP detection in CG (92).

2. MRI PRINCIPLES AND IMAGING TECHNIQUES



(a) DW-MRI image acquired with a 1.5 Tesla MRI scanner. The cancer corresponds to the high SI region highlighted in red.



(b) ADC map computer after acquisition of DW-MRI images with a 1.5 Tesla MRI scanner. The cancer corresponds to the low SI region highlighted in red.

Figure 2.4: Illustration of DW-MRI and ADC map. The signal intensity corresponding to cancer are inversely correlated on these two types of imaging techniques.

2.2.4 DW MRI

As previously mentioned in the introduction, DW MRI is the most recent MRI imaging technique aiming at CaP detection and diagnosis (64). This modality exploits the variations in the motion of water molecules in different tissues (103, 104).

From a physiological point of view, the following facts can be claimed. On the one hand, PZ, as previously mentioned, is mainly glandular and tubular in structure allowing water molecules to move freely (5, 34). On the other hand, CG is made up of muscular or fibrous tissue causing the motion of the water molecules to be more constrained and heterogeneous than in PZ (34). Then, CaP growth leads to the destruction of normal glandular structure and is associated with an increase in cellular density (34, 104, 105). Furthermore, these factors both have been shown to be inversely correlated with water diffusion (104, 105): higher cellular density implies a restricted water diffusion. Thus, water diffusion in CaP will be more restricted than both healthy PZ and CG (34, 104).

From the NMR principle side, DW MRI sequence produces contrasted images due to variation of water molecules motion. The method is based on the fact that the signal in DW MRI images is inversely correlated to the degree of random motion of water molecules (75). In fact, gradients are used in DW MRI modality to encode spatial

location of nuclei temporarily. Simplifying the problem in only one direction, a gradient is applied in that direction, dephasing the spins of water nuclei. Hence, the spin phases vary along the gradient direction depending of the gradient intensity at those locations. Then, a second gradient is applied aiming at cancelling the spin dephasing. Thus, the immobile water molecules will be subject to the same gradient intensity as the initial one while moving water molecules will be subject to a different gradient intensity. Thus, spins of moving water molecules will stay dephased whereas spins of immobile water molecules will come back in phase. As a consequence, a higher degree of random motion results in a more significant signal loss whereas a lower degree of random motion is synonymous with lower signal loss (75). Under these conditions, the MRI signal is measured as:

$$M_{x,y}(t, b) = M_{x,y}(0) \exp\left(-\frac{t}{T_2}\right) S_{\text{ADC}}(b) , \quad (2.3)$$

$$S_{\text{ADC}}(b) = \exp(-b \times \text{ADC}) , \quad (2.4)$$

where S_{ADC} refers to signal drop due to diffusion effect, ADC is the apparent diffusion coefficient and b is the attenuation coefficient depending only on gradient pulses parameters: (i) gradient intensity and (ii) gradient duration (106).

By using this formulation, image acquisition with a parameter $b = 0 \text{ s.mm}^{-2}$ corresponds to a T_2 -W MRI acquisition. Then, increasing the attenuation coefficient b (cf., increase gradient intensity and duration) enhances the contrast in DW MRI images.

To summarize, in DW MRI images, CaPs are characterized by high-SI compared to normal tissues in PZ and CG as shown in Fig. 2.4(a) (35). However, some tissues in CG can look similar to CaP with higher SI (35).

Diagnosis using DW MRI combined with T_2 -W MRI has shown a significant improvement compared with T_2 -W MRI alone and provides highly contrasted images (5, 107, 108). As drawbacks, this modality suffers from poor spatial resolution and specificity due to false positive detection (5). With a view to eliminate these drawbacks, radiologists are extracting quantitative maps from DW MRI. This imaging technique is presented next.

2.2.5 ADC Map

The NMR signal measured for DW MRI images is not only affected by diffusion as shown in Eq. (2.3). However, the signal drop (Eq. (2.4)) is formulated such that the only variable is the acquisition parameter b (106). The ADC is considered as a “pure” diffusion coefficient and can be extracted to build a quantitative map.

From Eq. (2.3), it is clear that performing multiple acquisitions only varying b will not have any effect on the term $M_{x,y}(0) \exp\left(-\frac{t}{T_2}\right)$. Thus, Eq. (2.3) can be rewritten as:

$$S(b) = S_0 \exp(-b \times \text{ADC}) . \quad (2.5)$$

To compute the ADC map, a minimum of two acquisitions are necessary: (i) for $b_0 = 0 \text{ s.mm}^{-2}$ where the measured signal is equal to S_0 , and (ii) $b_1 > 0 \text{ s.mm}^{-2}$ (typically 1000 s.mm^{-2}). Then, the ADC map can be computed as:

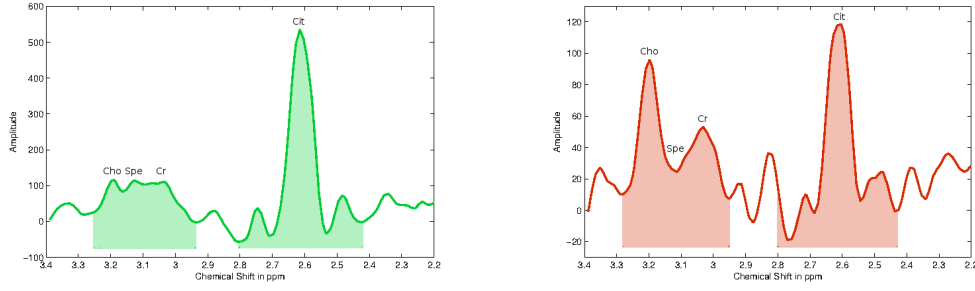
$$\text{ADC} = -\frac{\ln\left(\frac{S(b_1)}{S_0}\right)}{b_1} . \quad (2.6)$$

More accurate computation of the ADC map can be obtained by performing several acquisitions with different values for the parameter b and performing a semi-logarithmic linear fitting using the model presented in Eq. (2.5).

Regarding the appearance of the ADC maps, it was previously stated that by increasing the value of b , the signal of CaP tissue increases significantly. From Eq. (2.6), it can be shown that tissue appearance in the ADC map will be the inverse of DW MRI images. Then, CaP tissue is associated with low-SI whereas healthy tissue appears brighter as depicted in Fig. 2.4(b) (35).

Similar to the gain achieved by DW MRI, diagnosis using ADC map combined with T₂-W MRI significantly outperforms T₂-W MRI alone (5, 109). Moreover, it has been shown that ADC is correlated with GS (76, 77, 78).

However, some tissues of the CG zone mimic CaP with low-SI (84) and image distortion can arise due to haemorrhage (5). It has also been noted that a high variability of the ADC occurs between different patients making it difficult to define a static threshold to distinguish CaP from non-malignant tumours (5).



(a) Illustration of an MRSI spectrum of an healthy voxel acquired with a 3.0 Tesla MRI.

(b) Illustration of an MRSI spectrum of a cancerous voxel acquired with a 3.0 Tesla MRI.

Figure 2.5: Illustration of an MRSI spectrum both healthy and cancerous voxel with a 3.0 Tesla MRI. The highlighted areas corresponds to the related concentration of the metabolites which is computed by integrating the area under each peak. Acronyms: Choline (Cho), Spermine (Spe), Creatine (Cr) and Citrate (Cit).

2.2.6 MRSI

CaP induces metabolic changes in the prostate compared with healthy tissue. Thus, CaP detection can be carried out by tracking changes of metabolite concentration in prostate tissue. MRSI is an NMR-based technique which generates spectra of relative metabolite concentration in a ROI.

In order to track changes of metabolite concentration, it is important to know which metabolites are associated with CaP. To address this question, clinical studies identified three biological markers: (i) citrate, (ii) choline and (iii) polyamines composed mainly of spermine, and in less abundance of spermidine and putrescine (80, 81, 83).

Citrate is involved in the production and secretion of the prostatic fluid, and the glandular prostate cells are associated with a high production of citrate enabled by zinc accumulation by these same cells (81). However, the metabolism allowing the accumulation of citrate requires a large amount of energy (81). In contrast, malignant cells do not have high zinc levels leading to lower citrate levels due to citrate oxydation (81). Furthermore, this change results in a more energy-efficient metabolism enabling malignant cells to grow and spread (81).

An increased concentration of choline is related to CaP (80). Malignant cell development requires epigenetic mechanisms resulting in metabolic changes and relies on two mechanisms: DNA methylation and phospholipid metabolism which both result in choline

2. MRI PRINCIPLES AND IMAGING TECHNIQUES

uptake, explaining its increased level in CaP tissue (80). Spermine is also considered as a biological marker in CaP (82, 83). In CaP, reduction of the ductal volume due to shifts in polyamine homeostasis might lead to a reduced spermine concentration (82).

To determine the concentration of these biological markers, one has to focus on the MRSI modality. In theory, in presence of a homogeneous magnetic field, identical nuclei precesses at the same operating frequency known as the Larmor frequency (110). However, MRSI is based on the fact that identical nuclei will slightly precess at different frequencies depending on the chemical environment in which they are immersed (110), a phenomenon known as the chemical shift effect (CSE) (7). Given this property, metabolites can be identified and their concentrations can be determined. In this regard, the Fourier transform is used to obtain the frequency spectrum of the NMR signal (7, 110). In this spectrum, each peak is associated with a particular metabolite and the area under each peak corresponds to the relative concentration of this metabolite (see Fig. 2.5) (7).

Two different quantitative approaches are used to decide or whether not the spectra of a ROI is associated with CaP classified either as relative quantification or absolute quantification (111). In relative quantification, the ratio of choline-polyamines-creatine to citrate is computed. The integral of the signal is computed from choline (cf., 3.21 ppm) to creatine (cf., 3.02 ppm) because the peaks in this region can be merged at clinical magnetic field strengths (see Fig. 2.5) (34, 82). Considering the previous assumption that choline concentration rises and citrate concentration decreases in the presence of CaP, the ratio computed should be higher in malignant tissue than in healthy tissue.

Two different quantitative approaches are used to decide or not the spectra of a ROI is associated with CaP classified either as relative quantification or absolute quantification (111). In relative quantification, the ratio of choline-polyamines-creatine to citrate is computed. The integral of the signal is computed from choline (cf., 3.21 ppm) to creatine (cf., 3.02 ppm) because the peaks in this region can be merged at clinical magnetic field strengths (see Fig. 2.5) (34, 82). Considering the previous assumption that choline concentration rises and citrate concentration decreases in the presence of CaP, the ratio computed should be higher in malignant tissue than in healthy tissue.

In contrast with relative quantification, absolute quantification measures molar concentrations by normalizing relative concentrations using water as reference (111). In this case, “true” concentrations are directly used to differentiate malignant from healthy

tissue. However, this method is not commonly used as it requires an additional step of acquiring water signals, inducing time and cost acquisition constraints.

MRSI allows examination with high specificity and sensitivity compared to other MRI modalities (5). Furthermore, it has been shown that combining MRSI with MRI improves detection and diagnosis performance (112, 113, 114). Citrate and spermine concentrations are inversely correlated with the GS allowing us to distinguish low from high grade CaPs (83). However, choline concentration does not provide the same properties (83).

Unfortunately, MRSI also presents several drawbacks. First, MRSI acquisition is time consuming which prevents this modality from being used in daily clinical practise (35). In addition, MRSI suffers from low spatial resolution due to the fact that signal-to-noise (SNR) is linked to the voxel size. However, this issue is addressed by developing new scanners with higher magnetic field strengths such as 7.5 T (83). Finally, a high variability of the relative concentrations between patients was observed (5). The same observation was made depending on the zones studied (cf., PZ, CG, base, mid-gland, apex) (111, 115). Due to this variability, it is difficult to use a fixed thresholds in order to differentiate CaP from healthy tissue.

2. MRI PRINCIPLES AND IMAGING TECHNIQUES

Chapter 3

Review of CADe and CADx for CaP

As previously mentioned in the introduction (see Sect. 1.4), CADs are developed to advise and backup radiologists in their tasks of CaP detection and diagnosis, but not to provide fully automatic decisions (54). CADs can be divided into two different subgroups either as CADe, with the purpose to highlight probable lesions in MRI images, or CADx, which focuses on differentiating malignant from non-malignant tumours (54). Moreover, an intuitive approach, motivated by developing a framework combining detection-diagnosis, is to mix both CADe and CADx by using the output of the former mentioned as a input of the latter named. Although the outcomes of these two systems should differ, the framework of both CAD systems is similar. A general CAD work-flow is presented in Fig. 2.1.

MRI modalities mentioned in Sect. ?? are used as inputs of CAD for CaP. These images acquired from the different modalities show a large variability between patients: the prostate organ can be located at different positions in images (e.g., patient motion, variation of acquisition plan), and the SI can be corrupted with noise or artefacts during the acquisition process (eg., magnetic field inhomogeneity, use of endorectal coil). To address these issues, the first stage of CAD is to pre-process multiparametric MRI images to reduce noise, remove artefacts and standardize the SI. At most of the later processes will be only focused on the prostate, it is necessary to segment the prostate in each MRI-modality to define it as a ROI. However, data may suffer from misalignment due to patient motions or different acquisition parameters. Therefore, a registration step

3. REVIEW OF CADE AND CADX FOR CAP

is usually performed so that all the previously segmented MRI images will be in the same reference frame. Registration and segmentation can be swapped depending on the strategy chosen.

Some studies do not fully apply the methodology depicted in Fig.. 2.1. Details about those can be found in Tab. 3.1. Some studies proposed methods in which inputs are the MRI raw data inorder to demonstrate the robustness of their approaches to noise or artefacts. In some cases, prostate segmentation is performed manually as well as registration. It is also sometimes assumed that no patient motions occur during the acquisition procedure, removing the need of registering the multiparametric MRI images.

Once the data are regularized, it becomes possible to extract features and classify the data to obtain either the location of possible lesions (CADE) or/and the malignancy nature of these lesions (CADx).

In a CADE framework, *possible lesions will be segmented automatically* and further used as input of CADx. Nevertheless, some works also used a fusion CADE-CADx framework in which a voxel-based features are directly used, allowing to obtain the location of the malignant lesions as results. On the other hand, manual lesions segmentation are not considered to be part of CADE. The output of the CADE is used as input of the CADx.

CADx is composed of the processes allowing to *distinguish malignant from non-malignant tumours*. Here, CaP malignancy is defined using the grade of the GS determined after post biopsy or prostatectomy. As presented in Fig.. 2.1, CADx is usually composed of the three common steps used in classification framework: (i) features detection, (ii) feature extraction/selection and (iii) feature classification.

This chapter is organized using the methodology presented in Fig.. 2.1. Methods embedded in the image regularization framework are presented initially to subsequently focus on the image classification framework, being divided into CADE and CADx. Table 3.1 summarizes the fourty-two different CAD studies reviewed in section. The first set of information reported is linked to the data acquisition such as the number of patients included in the study, the modalities acquired as well as the strength of the field of the scanner used. Subsequently, information about the prostate zones considered in the CAD analysis (PZ or CG) are reported since that detecting CaP in the CG is a more challenging problem and has received particular attention only in the recent publications.

Table 3.1: Overview of the different studies reviewed with their main characteristics. Acronyms: number (#) - image regularization (Img. Reg.).

Index	Study	# Cases	MRI-modality				Strength of field		Studied zones		CAD stages		
			T ₂ -W	DCE	DW	MRSI	1.5 T	3.0 T	PZ	CG	Reg.	CADe	CADx
(116)	Ampeliotis et al. (2007)	25	✓	✓	✗	✗	✓	✗	✓	✗	✓!	✗	✓
(117)	Ampeliotis et al. (2008)	25	✓	✓	✗	✗	✓	✗	✓	✗	✓!	✗	✓
(118)	Antic et al. (2013)	53	✓	✗	✓	✗	✓	✗	✓	✓	✗	✗	✓
(119)	Artan et al. (2009)	10	✓	✓	✓	✗	✓	✗	✓	✗	✗	✓	✓
(120)	Artan et al. (2010)	21	✓	✓	✓	✗	✓	✗	✓	✗	✓!	✓	✓
(121)	Chan et al. (2013)	15	✓	✗	✓	✗	✓	✗	✓	✗	✗	✗	✓
(122)	Giannini et al. (2013)	10	✓	✓	✓	✗	✓	✗	✓	✗	✓	✓	✓
(123)	Kelm et al. (2007)	24	✗	✗	✗	✓	✓	✗	✓	✓	✓!	✓	✓
(124)	Langer et al. (2009)	25	✓	✓	✓	✗	✓	✗	✓	✗	✓!	✗	✓
(125)	Litjens et al. (2011)	188	✓	✓	✓	✗	✗	✓	✓	✗	✓!	✓	✓
(126)	Litjens et al. (2012)	288	✓	✓	✓	✗	✗	✓	✓	✓	✓!	✓	✓
(127)	Litjens et al. (2014)	347	✓	✓	✓	✗	✗	✓	✓	✓	✓!	✓	✓
(128)	Liu et al. (2009)	11	✓	✓	✓	✗	✓	✗	✓	✗	✓!	✓	✓
(129)	Liu et al. (2013)	54	✓	✓	✓	✗	✗	✓	✓	✓	✓!	✗	✓
(130)	Lopes et al. (2011)	27	✓	✗	✗	✗	✓	✗	✓	✗	✓!	✓	✓
(131)	Lv et al. (2009)	55	✓	✗	✗	✗	✓	✗	✓	✗	✓!	✗	✓
(132)	Matulewicz et al. (2013)	18	✗	✗	✗	✓	✗	✓	✓	✓	✗	✓	✓
(133)	Mazzetti et al. (2011)	10	✗	✓	✗	✗	✓	✗	✓	✗	✓!	✓	✓
(2)	Niaf et al. (2011)	23	✓	✓	✓	✗	✓	✗	✓	✗	✓!	✗	✓
(3)	Niaf et al. (2012)	30	✓	✓	✓	✗	✓	✗	✓	✗	✓!	✗	✓
(134)	Ozer et al. (2009)	20	✓	✓	✓	✗	✓	✗	✓	✗	✓!	✓	✓
(135)	Ozer et al. (2010)	20	✓	✓	✓	✗	✓	✗	✓	✗	✓!	✓	✓
(136)	Parfait et al. (2012)	22	✗	✗	✗	✓	✗	✓	✓	✓	✓!	✓	✓
(78)	Peng et al. (2013)	48	✓	✓	✓	✗	✗	✓	✓	✓	✗	✗	✓
(137)	Puech et al. (2009)	100	✗	✓	✗	✗	✓	✗	✓	✓	✗	✗	✓
(138)	Sung et al. (2011)	42	✗	✓	✗	✗	✗	✓	✓	✓	✗	✓	✓
(139)	Tiwari et al. (2007)	14	✗	✗	✗	✓	✓	✗	✓	✓	✓!	✓	✓
(140)	Tiwari et al. (2008)	18	✗	✗	✗	✓	✓	✗	✓	✓	✓!	✓	✓
(141)	Tiwari et al. (2009)	18	✗	✗	✗	✓	✓	✗	✓	✓	✓!	✓	✓
(142)	Tiwari et al. (2009)	15	✓	✗	✗	✓	✓	✗	✓	✓	✓!	✓	✓
(143)	Tiwari et al. (2010)	19	✓	✗	✗	✓	✓	✗	✓	✓	✓!	✓	✓
(144)	Tiwari et al. (2012)	36	✓	✗	✗	✓	✓	✗	✓	✓	✗	✓	✓
(145)	Tiwari et al. (2013)	29	✓	✗	✗	✓	✓	✗	✓	✓	✓!	✓	✓
(146)	Viswanath et al. (2008)	16	✓	✗	✗	✓	✓	✗	✓	✓	✗	✓	✓
(147)	Viswanath et al. (2008)	6	✓	✓	✗	✗	✗	✓	✓	✓	✓!	✓	✓
(148)	Viswanath et al. (2009)	6	✓	✓	✗	✗	✗	✓	✓	✓	✓	✓	✓
(149)	Viswanath et al. (2011)	12	✓	✓	✓	✗	✗	✓	✓	✓	✓!	✓	✓
(150)	Viswanath et al. (2012)	22	✓	✗	✗	✗	✗	✓	✓	✓	✓	✓	✓
(151)	Vos et al. (2008)	29	✓	✓	✗	✗	✓	✗	✓	✗	✓!	✗	✓
(152)	Vos et al. (2008)	29	✗	✓	✗	✗	✓	✗	✓	✗	✓!	✗	✓
(153)	Vos et al. (2010)	29	✓	✓	✗	✗	✓	✗	✓	✗	✓!	✗	✓
(154)	Vos et al. (2012)	NA	✓	✓	✓	✗	✗	✓	✓	✗	✓!	✓	✓

Notes:

✗: not used or not implemented.

✓!: partially implemented.

✓: used or implemented.

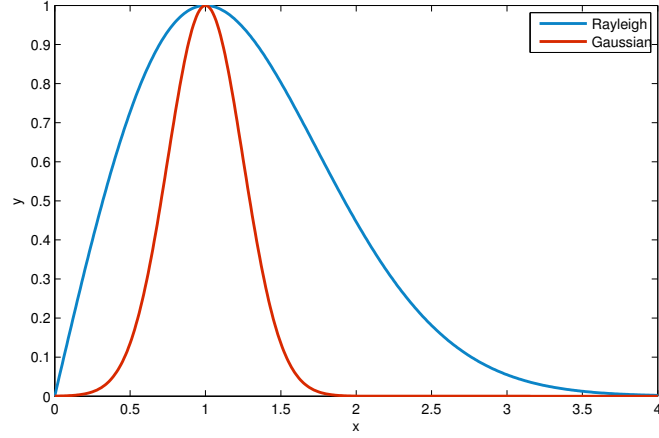


Figure 3.1: Illustration of a Gaussian distribution ($\mu = 1, \sigma = 0.25$) and a Rayleigh distribution ($\sigma = 2$). It can be seen that the Rayleigh distribution is suffering of a bias term when compared with the Gaussian distribution.

3.1 Image regularization framework

This section provides a review of the methods used in CADs for CaP in order to regularize input images. We start with pre-processing methods presented in Sect. 3.1.1, focusing mainly on the reduction of noise level and artefacts as well as standardization of SI. Sections 3.1.2 and ?? will be dedicated to segmentation methods, so that later methods only operate on the segmented prostate, and registration to align segmented images from different MRI-modalities in the same reference frame.

3.1.1 Pre-processing

Three different groups of pre-processing methods are commonly applied to images as initial stage in CAD for CaP. These methods are explained for both MRI and MRSI modalities, while a summary of the applied methods in CAD is presented in Table. 3.2.

Noise filtering: The NMR signal measured and recorded in the k-space during an MRI acquisition is affected by noise. This noise obeys a complex Gaussian white noise mainly due to thermal noises in the patient area (155). Furthermore, MRI images visualized by radiologists are in fact the magnitude images resulting from the complex Fourier transform of the k-space data. The complex Fourier transform, being a linear and orthogonal transform, does not affect the Gaussian noise characteristics (155). However, the function involved in the magnitude computation is a non-linear transform (i.e., the square root of the sum of squares of real and the imaginary parts), implying that the noise distribution is no longer Gaussian; it indeed follows a Rician distribution making the denoising task harder. Briefly, a Rician distribution can be characterized as follows:

in low-SI region (low SNR), it can be approximated with a Rayleigh distribution while in high-SI region (high SNR), it is similar to a Gaussian distribution (see Fig. 3.1) (156). Reviews of all denoising methods can be found in (157, 158).

Median filtering is the simplest approach used to address the denoising issue in MRI images (134, 135). In both studies, Ozer *et al.* used a square kernel of size 5×5 pixels with the image resolutions ranging from 320×256 (cf., T₂-W MRI) to 256×128 (cf., T₂ map, DCE and DW MRI) and a field of view (FOV) ranging from 14 cm (cf, T₂-W and DW MRI) to 20 cm (cf, T₂ map and DCE MRI). However, from a theoretical point of view, this simple filtering method is not well formalized to address the noise distribution in MRI images.

More complex approaches were proposed to overcome this problem. A common method used to denoise MRI images is based on wavelet-based filtering. This filtering exploits the sparsity property of the wavelet decomposition. The projection of a noisy signal from the spatial-domain to the wavelet-domain implies that only few wavelet coefficients contribute to the “signal-free noise” while all wavelet coefficients contribute to the noise (159). Therefore, denoising is performed by thresholding/attenuating the insignificant wavelet coefficients to enforce the sparsity in the wavelet-domain. Investigations focus on the strategies to perform the most adequate coefficient shrinkage method (e.g., using thresholding, singularity property or Bayesian framework) (160).

Ampeliotis *et al.* in (116, 117) performed wavelet shrinkage to denoise magnitude MRI images (cf., T₂-W-MRI and DCE-MRI) using thresholding techniques (161). However, since the wavelet transform is an orthogonal transform, the Rician distribution of the noise is preserved in the wavelet-domain. Hence, for low SNR, the wavelet and scaling coefficients still suffer from a bias due to this specific noise distribution (155).

Lopes *et al.* in (130) used the filtering technique proposed by (162) to denoise T₂-W-MRI which was based on joint detection and estimation theory (162). In this approach, the wavelet coefficients “free-of-noise” are estimated from the noisy wavelet coefficients using a maximum *a posteriori* (MAP) estimate. Furthermore, the estimator designed takes spatial context into account by including both local and global information in the prior probabilities. The different probabilities needed by the MAP are empirically estimated by using mask images representing the locations of the significant wavelet coefficients. These mask images are computed by thresholding the detail images obtained from the wavelet decomposition. To remove the bias from the wavelet and scaling coefficients, the squared magnitude MRI image used instead of the magnitude MRI image as proposed by (155). This involves changing the Rician distribution to a scaled non-central Chi-square distribution. It implies that the wavelet coefficients are also unbiased estimators and the scaling coefficients are unbiased estimators but up to a constant C as defined in Eq. (3.1) which needs to be subtracted from each scaling coefficient,

$$C = 2^{(J+1)}\hat{\sigma}^2, \quad (3.1)$$

where J is the number of levels of the wavelet decomposition and $\hat{\sigma}$ is an estimate of the noise standard deviation.

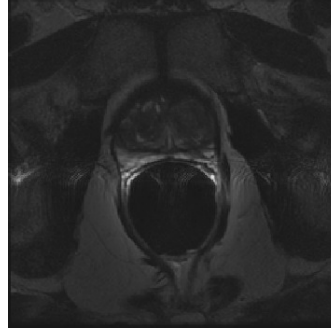


Figure 3.2: Example of artefacts with high SI due to perturbation from the endorectal coil which create inhomogeneity.

Bias correction: Besides being corrupted by noise, MRI images are also affected by the inhomogeneity of the MRI field commonly referred to as bias field (163). This bias field results in a smooth variation of the SI through the image. When an endorectal coil is used, an artefact resulting of an hyper-intense signal can be observed around the coil on the images (see Fig. 3.2).

As a consequence, the SI of identical tissues varies depending on their spatial location in the image making further processes such as segmentation or registration harder (164, 165). A review of bias correction methods can be found in (165).

The model of image formation is usually formalized such that:

$$s(\mathbf{x}) = o(\mathbf{x})b(\mathbf{x}) + \eta(\mathbf{x}) , \quad (3.2)$$

where $s(\mathbf{x})$ is the corrupted SI at the pixel for the image coordinates $\mathbf{x} = \{x, y\}$, $o(\mathbf{x})$ is the “noise-free signal” , $b(\mathbf{x})$ is the bias field function and $\eta(\mathbf{x})$ is an additive white Gaussian noise.

Hence, the task of bias correction involves estimating the bias function $b(\mathbf{x})$ in order to infer the “signal-free bias” $o(\mathbf{x})$.

Viswanath *et al.* (148) performed bias correction on T₂-W-MRI using a parametric Legendre polynomial model proposed in (163) and available in the Insight Segmentation and Registration Toolkit (ITK) library¹.

Styner *et al.* (163) chose to model the bias field by using a linear combination of Legendre polynomials as:

$$\hat{b}(\mathbf{x}, \mathbf{p}) = \sum_{i=0}^{m-1} p_i f_i(\mathbf{x}) = \sum_{i=0}^l \sum_{j=0}^{l-i} p_{ij} P_i(x) P_j(y) , \quad (3.3)$$

where \hat{b} is the bias estimation with the image coordinates $\mathbf{x} = \{x, y\}$ and the m coefficients of the linear combination $\mathbf{p} = p_{11}, \dots, p_{ij}$; m can be defined as $m = (l + 1) \frac{(l+2)}{2}$

¹The ITK library is available at: <http://www.itk.org/>

where l is the degree of Legendre polynomials chosen and $P_i(\cdot)$ denotes a Legendre polynomial of degree i .

This family of functions allows us to model the bias as a smooth inhomogeneity function across the image. To estimate the set of parameters \mathbf{p} , a cost function is defined which relies on the following assumptions: (i) an image is composed of k regions with μ_k being the mean SI and a variance σ_k^2 of each particular class, and (ii) each noisy pixel belongs to one of the k regions with its SI value close to the class mean μ_k . Hence, the cost function is defined as:

$$C(\mathbf{p}) = \sum_{\mathbf{x}} \prod_k \rho_k(s(\mathbf{x}) - \hat{b}(\mathbf{x}, \mathbf{p}) - \mu_k) , \quad (3.4)$$

$$\rho_k(x) = \frac{x^2}{x^2 + 3\sigma_k^2} , \quad (3.5)$$

where $\rho_k(\cdot)$ is a M-estimator allowing estimations to be less sensitive to outliers than usual square distance (166).

Finally, estimation of the parameters \mathbf{p} results in finding the minimum of the cost function $C(\mathbf{p})$. This optimization was performed using the non-linear (1 + 1) Evolution Strategy (ES) optimizer (167).

In a later publication, (150) make use of the well known N3 algorithm¹ to correct T₂-W-MRI developed by (168). To estimate the bias function, (168) proposed to estimate the probability density functions (PDFs) of the signal and bias.

Recalling Eq. (3.2) and taking advantage of logarithm property, it implies that this model becomes additive such that:

$$\begin{aligned} \log s(\mathbf{x}) &= \log b(\mathbf{x}) + \log \left(o(\mathbf{x}) + \frac{\eta(\mathbf{x})}{b(\mathbf{x})} \right) , \\ &\approx \log b(\mathbf{x}) + \log \hat{o}(\mathbf{x}) , \end{aligned} \quad (3.6)$$

where $\hat{o}(\mathbf{x})$ is the signal only degraded by noise. (168) shows that Eq. (3.6) can be related to PDFs such that:

$$S(s) = B(s) * O(s) , \quad (3.7)$$

where S , B and O are respectively the probability densities of s , b and o .

Restoring the corrupted signal s is carried out by finding the multiplicative field b which maximizes the frequency content of the distribution O . Sled *et al.* (168) argue that a search through all possible fields b and selection of the one which maximizes the high frequency content of O could be carried out but results in an exhaustive search. However, they show that the bias field distribution can be assimilated to a near Gaussian distribution. Using this fact as *a priori*, it is then possible to infer the distribution O

¹The N3 algorithm implementation is available at: <http://www.bic.mni.mcgill.ca/software/N3/>

3. REVIEW OF CADE AND CADX FOR CAP

using Wiener deconvolution given B and S and later estimate the corresponding smooth field b .

Lv *et al.* (131) corrected the inhomogeneity in T₂-W-MRI images by using the method proposed in (169). In this method, the MRI images are corrected iteratively by successively detecting the image foreground via generalized scale (g -scale) and estimating a bias field function based on a second-order polynomial model. First the background of the MRI image is eliminated by thresholding. The threshold value is commonly equal to the mean SI of the considered image. Then, in the seeded region growing algorithm is applied considering every thresholded pixel as a potential seed. However, pixels already assigned to a region will not be considered any more as seed. As in seeded region growing algorithm (170), two criteria are taken into account to expand the region. First, the region will grow using a connected-neighbourhood, initially defined by the user. Then, the homogeneity of SI is based on a fuzzy membership function taking into account the absolute difference of the SIs of two pixels. Depending on the membership value (cf., a threshold has to be defined), the pixel considered is merged or not to the region. Once this segmentation is performed, the largest region R is used as a mask to select pixels of the original image and the mean SI, μ_R , is computed. The background variation $b(\mathbf{x})$ is estimated as:

$$b(\mathbf{x}) = \frac{s(\mathbf{x})}{\mu_R}, \quad \forall \mathbf{x} \in R, \quad (3.8)$$

where $s(\mathbf{x})$ is the original MRI image.

Finally, a second order polynomial $\hat{b}_\Theta(\mathbf{x})$ is fitted in a least-squares sense (Eq. (3.9)),

$$\hat{\Theta} = \arg \min_{\Theta} |b(\mathbf{x}) - \hat{b}_\Theta(\mathbf{x})|^2, \quad \forall \mathbf{x} \in R. \quad (3.9)$$

Finally, the whole original MRI image is corrected by dividing it by the estimated bias field function $\hat{b}_\Theta(\mathbf{x})$. This process is repeated until the number of pixels in the largest region R does not change significantly between two iterations.

SI normalization/standardization: As discussed in the later section, segmentation or classification tasks are usually performed by first learning from a training set of patients. Hence, one can emphasize the desire to perform MRI examinations with a high repeatability or in other words, one would ensure to obtain similar MRI images (cf., similar SIs) for patients of the same group (cf., healthy patients *vs.* patients with CaP), for a similar sequence.

However, it is a known fact that variability between patients occurs during the MRI examinations even using the same scanner, protocol or sequence parameters (171). Hence, the aim of normalization or standardization of the MRI data is to remove the variability between patients and enforce the repeatability of the MRI examinations. Approaches used to standardize MRI images can be either categorized as statistical-based standardization or organ SI-based standardization.

3.1 Image regularization framework

Artan *et al.* (119, 120) as well as Ozer *et al.* (134, 135) standardized T₂-W, DCE and DW MRI images by computing the *standard score* (also called *z-score*) of the pixels of the PZ as:

$$I_s(\mathbf{x}) = \frac{I_r(\mathbf{x}) - \mu_{pz}}{\sigma_{pz}}, \quad \forall \mathbf{x} \in \text{PZ}, \quad (3.10)$$

where $I_s(\mathbf{x})$ is the standardized SI with the image coordinates $\mathbf{x} = \{x, y\}$, $I_r(\mathbf{x})$ is the raw SI, μ_{pz} is the mean-SI of the PZ and σ_{pz} is the SI standard deviation in the PZ. This transformation enforces the image PDF to have a zero mean and a unit standard deviation.

In a similar way, Liu *et al.* (129) normalized T₂-W-MRI by making use of the median and interquartile range for all the pixels.

Lv *et al.* (131) scaled the SI of T₂-W-MRI images using the method proposed in (1) based on PDF matching. This approach is based on the assumption that MRI images from the same sequence should share the same PDF appearance. Hence, one can approach this issue by transforming and matching the PDFs using some statistical landmarks such as median and different quantiles. Using a training set, these statistical landmarks are extracted for N training images as for instance for the minimum, the 25th quantile, the median, the 75th quantile and the maximum:

$$\begin{aligned} \Phi_0 &= \{\phi_0^1, \phi_0^2, \dots, \phi_0^N\}, \\ \Phi_{25} &= \{\phi_{25}^1, \phi_{25}^2, \dots, \phi_{25}^N\}, \\ \Phi_{50} &= \{\phi_{50}^1, \phi_{50}^2, \dots, \phi_{50}^N\}, \\ \Phi_{75} &= \{\phi_{75}^1, \phi_{75}^2, \dots, \phi_{75}^N\}, \\ \Phi_{100} &= \{\phi_{100}^1, \phi_{100}^2, \dots, \phi_{100}^N\}, \end{aligned} \quad (3.11)$$

where $\phi_n^{i^{\text{th}}}$ is the n^{th} quantile of the i^{th} training image.

Then, the mean of each quantile $\{\bar{\Phi}_0, \bar{\Phi}_{25}, \bar{\Phi}_{50}, \bar{\Phi}_{75}, \bar{\Phi}_{100}\}$ is also calculated. Once this training stage is performed, a linear transformation by parts $\mathcal{T}(\cdot)$ can be computed (Eq. (3.12)) for each test image t by mapping each statistical landmark $\varphi_{(\text{cdot})}^t$ of this image with the pre-learned statistical landmarks $\bar{\Phi}_{(\cdot)}$. This linear mapping is also depicted in Fig. 3.3.

$$\mathcal{T}(s(\mathbf{x})) = \begin{cases} \lceil \bar{\Phi}_0 + (s(\mathbf{x}) - \varphi_0^t) \left(\frac{\bar{\Phi}_{25} - \bar{\Phi}_0}{\varphi_{25}^t - \varphi_0^t} \right) \rceil, & \text{if } \varphi_0^t \leq s(\mathbf{x}) < \varphi_{25}^t, \\ \lceil \bar{\Phi}_{25} + (s(\mathbf{x}) - \varphi_{25}^t) \left(\frac{\bar{\Phi}_{50} - \bar{\Phi}_{25}}{\varphi_{50}^t - \varphi_{25}^t} \right) \rceil, & \text{if } \varphi_{25}^t \leq s(\mathbf{x}) < \varphi_{50}^t, \\ \lceil \bar{\Phi}_{50} + (s(\mathbf{x}) - \varphi_{50}^t) \left(\frac{\bar{\Phi}_{75} - \bar{\Phi}_{50}}{\varphi_{75}^t - \varphi_{50}^t} \right) \rceil, & \text{if } \varphi_{50}^t \leq s(\mathbf{x}) < \varphi_{75}^t, \\ \lceil \bar{\Phi}_{75} + (s(\mathbf{x}) - \varphi_{75}^t) \left(\frac{\bar{\Phi}_{100} - \bar{\Phi}_{75}}{\varphi_{100}^t - \varphi_{75}^t} \right) \rceil, & \text{if } \varphi_{75}^t \leq s(\mathbf{x}) \leq \varphi_{100}^t, \end{cases} \quad (3.12)$$

Viswanath *et al.* (148, 149, 150) use a variant of this previous approach presented in (172) aiming to standardize the T₂-W-MRI images. Instead of computing the PDF of an entire image, a pre-segmentation of the foreground is carried out via g -scale which

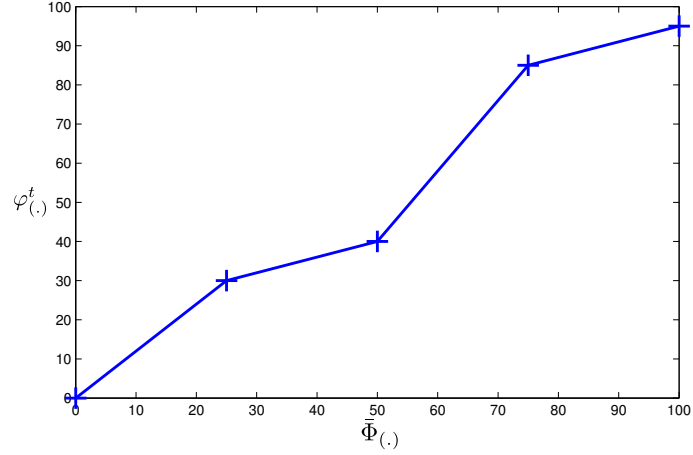


Figure 3.3: Example of linear mapping by parts as proposed by (1).

was discussed in the bias correction section. Once the foreground is detected, the largest region is extracted and the same process than previously mentioned (see Eq. (3.12)) takes place in order to align PDFs of the foreground of the MRI images.

The methods described above were statistical-based methods. However, the standardization problem can be tackled by normalizing the MRI images using the SI of some known organs present in these images. Niaf *et al.* (2, 3) normalized T₂-W-MRI images by dividing the original SI of the images by the mean SI of the bladder (see Fig. 3.4(a)). Likewise, (2) standardized the T₁-W-MRI images using the arterial input function (AIF). They computed the AIF by taking the mean of the SI in the most enhanced part of the common femoral arteries (see Fig. 3.4(b)) as proposed in (173).

Presented in Sect. 2.2.6, MRSI is a modality related to a one dimensional signal. Hence, specific pre-processing steps for this type of signals have been applied instead of standard signal processing methods.

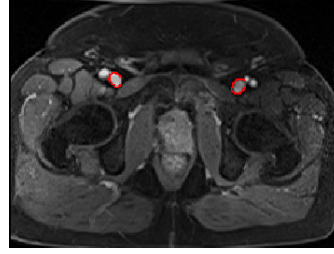
Phase correction: MRSI data acquired suffer from zero-order and first-order phase misalignments as shown in Fig. 3.5 (174, 175). Parfait *et al.* (136) used a method proposed in (174) where the phase of MRSI signal is corrected based on entropy minimization in the frequency domain. The corrected MRSI signal $o(\xi)$ can be expressed as:

$$\begin{aligned}
 \Re(o(\xi)) &= \Re(s(\xi)) \cos(\Phi(\xi)) - \Im(\xi) \sin(\Phi(\xi)) , \\
 \Im(o(\xi)) &= \Im(s(\xi)) \cos(\Phi(\xi)) + \Re(\xi) \sin(\Phi(\xi)) , \\
 \Phi(\xi) &= \phi_0 + \phi_1 \frac{\xi}{N} ,
 \end{aligned} \tag{3.13}$$

where $\Re(\cdot)$ and $\Im(\cdot)$ are the real and imaginary part of the complex signal respectively,



(a) Illustration and location of the bladder on a T_2 -W-MRI image acquired with a 3.0 Tesla MRI scanner



(b) Illustration and location of the femoral arteries on a T_1 -W-MRI image acquired with a 3.0 Tesla MRI scanner

Figure 3.4: Illustration of the two organs used by (2, 3) to normalize T_2 -W and T_1 -W MRI images.

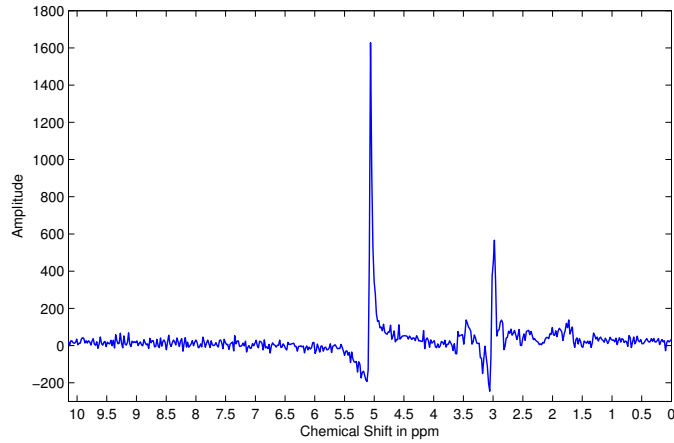


Figure 3.5: Illustration of phase misalignment in an MRSI spectra acquire with a 3.0 Tesla MRSI scanner. Note the distortion of the signal specially visible for the water and citrate peaks.

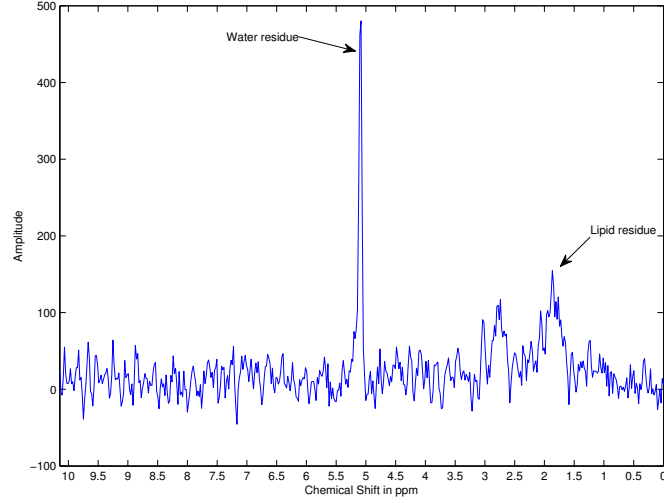


Figure 3.6: Illustration of the residues of water and fat even after their suppression during the acquisition protocol. The acquisition was carried out with a 3.0 Tesla MRI.

$s(\xi)$ is the corrupted MRSI signal, ϕ_0 and ϕ_1 are the zero-order and first-order phase correction terms respectively and N is the total number of samples of the MRSI signal.

Chen *et al.* (174) tackled this problem using an optimization framework where ϕ_0 and ϕ_1 had to be inferred. Hence, the simplex Nelder-Mead optimization method was used to minimize the following cost function based on the *Shannon entropy* formulation:

$$\hat{\Phi} = \arg \min_{\Phi} \left[- \sum \Re(s'(\xi)) \ln \Re(s'(\xi)) + \lambda \|\Re(s(\xi))\|_2 \right], \quad (3.14)$$

where $s'(\xi)$ is the first derivative of the corrupted signal $s(\xi)$ and λ is a regularization parameter. Once the best parameter Φ is obtained, the MRSI signal is corrected using Eq. (3.13).

Water and lipid residuals filtering: The water and lipid metabolites occur in much higher concentrations than the metabolites of interests (cf., choline, creatine and citrate) (175, 176). Fortunately, specific MRSI sequences were developed in order to suppress water and lipid metabolites using pre-saturation techniques (176). However, these techniques do not perfectly remove water and lipids peaks and some residuals are still present in the MRSI spectra as shown in Fig. 3.6. Therefore, different post-processing methods have been proposed to enhance the quality of the MRSI spectra by removing these residuals. For instance, Kelm *et al.* (123) used the well known HSVD algorithm proposed by (177) which models the MRSI signal by a sum of exponentially damped sinusoids in the time

domain (see Eq. (3.15)).

$$s(t) = \sum_{k=1}^K a_k \exp(i\phi_k) \exp(-d_k + i2\pi f_k)t + \eta(t) , \quad (3.15)$$

where a_k is the amplitude proportional to the metabolite concentration with a resonance frequency f_k , d_k represents the damping factor of the exponential, ϕ_k is the first-order phase and $\eta(t)$ is a complex white noise.

Pijnappel *et al.* (177) showed that the “noise-free signal” can be found using the singular value decomposition (SVD) decomposition. First the noisy signal is reorganized inside a Hankel matrix H . It can be shown that if the signal considered would be a “noise-free signal”, the rank of H would be equal to rank K . However, due to the presence of noise, H is in fact a full rank matrix. Thus, to recover the “noise-free signal”, the rank of H can be truncated to K using its SVD decomposition. Hence, knowing the cut off frequencies of water (cf., 4.7 ppm) and lipid (cf., 2.2 ppm) metabolites, their corresponding peaks can be reconstructed and subtracted from the original signal (178).

Baseline correction: Sometimes, the problem discussed in the above section regarding the lipid molecules is not addressed simultaneously with water residuals suppression. Lipids and macromolecules are known to affect the baseline of the MRSI spectra. They could cause errors during further fitting processes aiming to quantify the metabolites, especially regarding the citrate metabolite.

Parfait *et al.* (136) made the comparison of two different methods to detect the baseline and correct the MRSI spectra which are based on (179, 180). Lieber *et al.* (179) addressed the problem of baseline detection in the frequency domain by fitting a low degree polynomial whereas Parfait *et al.* (136) modified this algorithm by convolving a Gaussian kernel to smooth the MRSI signal instead of fitting a polynomial function.

Check the tex file to see the commented area pre-processing.tex

Unlike in (179), Devos *et al.* (180) proposed to correct the baseline in the time domain by multiplying the MRSI signal by a decreasing exponential function as:

$$c(t) = \exp(-\beta t) , \quad (3.16)$$

Having a typical value for β of 0.15. However, Parfait *et al.* (136) concluded that the method proposed in (179) outperformed the one in (180).

In the contemporary work of Tiwari *et al.* (144), the authors detected the baseline using a local non-linear fitting method avoiding regions with significant peaks which were detected using a experimentally parametrised signal-to-noise ratio (i.e. a value larger than 5 dB).

Frequency alignment: Due to variations of the experimental conditions, a frequency shift can be observed in the MRSI spectra (174, 175) as shown in Fig. 3.7.

3. REVIEW OF CADE AND CADX FOR CAP

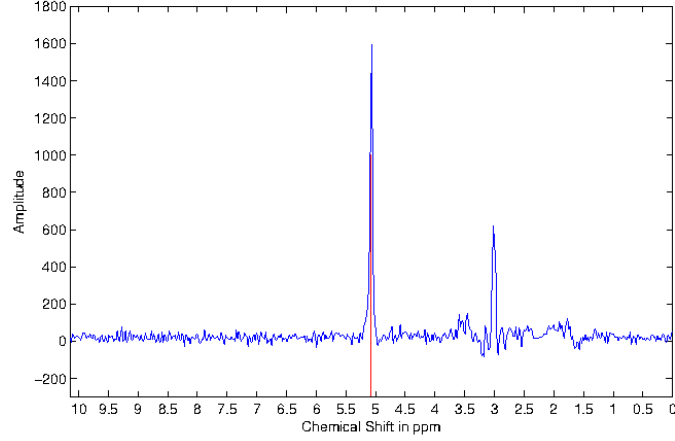


Figure 3.7: Illustration of frequency misalignment in an MRSI spectra acquired with a 3.0 Tesla MRSI scanner. The water peak is known to be aligned at 4.65 ppm. However, it can be seen that the peak on this spectra is aligned at around 5.1 ppm.

Tiwari *et al.* (144) corrected the frequency shift by first detecting known metabolite peaks such as choline, creatine and citrate. The frequency shift is corrected by minimizing the frequency error between the experimental and theoretical values of each of these peaks.

Normalization: Due to variations of the experimental conditions, the MRSI signal may also vary between patients. Parfait *et al.* (136) as in (180) compared two methods to normalize MRSI signal. In each method, the original MRSI spectra is divided by a normalization factor, similar to the intensity normalization described earlier. The first approach to obtain the normalization factor is based on an estimation of the water concentration. It is required to have an additional MRSI sequence where the water metabolites are unsuppressed. Using this sequence, an estimation of the water concentration can be performed using the previously reported HSVD algorithm. The second approach to normalization is based on using the L_2 norm of the MRSI spectra $\|s(\xi)\|_2$. It should be noted that both (136) and (180) concluded that the L_2 normalization was more efficient in their framework.

3.1.2 Segmentation

The segmentation task consists of delineating the prostate boundaries in the MRI and is of particular importance for focusing the posterior processing on the organ of interest (181). In this section, only the segmentation methods used in CAD for CaP are presented and summarized in Table. 3.3. These methods are mostly intensity based. An exhaustive review of prostate segmentation methods in MRI can be found in (181).

Table 3.2: Overview of the pre-processing methods used in CAD systems.

Pre-processing operations	References
<i>MRI pre-processing:</i>	
Noise filtering:	
Median filtering	(134, 135)
Wavelet-based filtering	(116, 117, 130)
Bias correction:	
Parametric methods	(131, 148)
Non-parametric methods	(149)
Standardization:	
Statistical-based normalization:	(119, 120, 131, 134, 135, 148, 149, 150)
Organ SI-based normalization	(2, 3)
<i>MRSI pre-processing:</i>	
Phase correction	(136)
Water and lipid residuals filtering	(123)
Baseline correction	(136, 144)
Frequency alignment	(144)
Normalization	(136)

Table 3.3: Overview of the segmentation methods used in CAD systems.

Segmentation methods	References
<i>MRI-based segmentation:</i>	
Manual segmentation	(2, 3, 119, 120, 132, 134, 135, 137, 151, 152, 153, 154)
Region-based segmentation	(126, 127)
Model-based segmentation	(125, 147, 148, 149, 154)
<i>MRSI-based segmentation:</i>	
Clustering	(141)

3. REVIEW OF CADE AND CADX FOR CAP

Manual segmentation: To highlight the importance of prostate segmentation task in CAD systems, it is interesting to note the large number of studies which manually segment the prostate organs (2, 3, 119, 120, 132, 134, 135, 137, 151, 152). In all the cases, the boundaries of the prostate gland are manually defined in order to limit further processing to only this area. This approach ensures the right delineation of the organ nevertheless this procedure is highly time consuming and should be performed by a radiologist.

Region-based segmentation: Litjens *et al.* in (126) used a multi-atlas-based segmentation using multi-modal images (e.g., T_2 -W-MRI and ADC map) to segment the prostate with an additional pattern recognition method to differentiate CG and PZ as proposed in (182). This method consists in three different steps: (i) the registration between each atlas and the multi-modal images, (ii) the atlas selection and finally (iii) the classification of the prostate segmented voxels in either CG or PZ. The registration between each atlas and the MRI images is performed using two successive registrations; the first registration is a rigid registration to roughly aligned the atlases and the MRI images and the second is an elastic registration using B-spline transformation. The objective function to perform the registration is defined as the weighted sum of the metric of both T_2 -W-MRI and ADC map. The metric is based on mutual information (MI) (please refer to the next section for more details in regard to registration). Two strategies of atlas selection were performed by using either a majority voting approach or the simultaneous truth and performance level estimation (STAPLE) approach (183).

Subsequently, CG and PZ segmentation within the prostate region is achieved by classifying each voxel using a linear discriminant analysis (LDA) classifier. Three types of features were considered: (i) anatomy, (ii) intensity and (iii) texture. Regarding the anatomy, relative position and relative distance from the pixel to the border of the prostate were used. The intensity features consist in the intensity of the voxel in the ADC coefficient and the T_2 map. The texture features were composed of five different features: homogeneity, correlation (184), entropy, texture strength (185) and local binary pattern (LBP) (186). Finally, some morphological operations were applied to remove artefact and the contour between the zones were smooth using the thin plate spline (TPS) (187).

Litjens *et al.* in (127) used an almost identical algorithm proposed by PROMISE12 challenge (188). Their segmentation method is also based on multi-atlas multi-modal images, but the SIMPLE method (189) is used instead to combine labels after the registration of the different atlas to obtain the final segmentation.

Model-based segmentation: Viswanath *et al.* in (147, 148) used a multi-attribute non-initializing texture reconstruction based active shape model (MANTRA) method as proposed in (190). MANTRA is closely related to the active shape model (ASM) from (191). This algorithm consists of two stages: (i) a training stage where a shape and appearance model is generated and (ii) the actual segmentation performed based on the learned model. For the training stage, a set of landmarks is defined and the shape model is generated as in the original ASM method (191). Then, to model the appearance, a set

of K texture images $\{I_1, I_2, \dots, I_k\}$ based on first and second order statistical texture features are computed. For a given landmark l with its given neighbourhood $\mathcal{N}(l)$, its feature matrix extracted can be expressed as:

$$f_l = \{I_1(\mathcal{N}(l)), I_2(\mathcal{N}(l)), \dots, I_k(\mathcal{N}(l))\}, \quad (3.17)$$

where $I_k(\mathcal{N}(l))$ represents a feature vector obtained by sampling the k^{th} texture map using the neighbourhood $\mathcal{N}(l)$. By generating multiple landmarks in the same fashion as ASM, principal components analysis (PCA) (192) is applied to learn the appearance variations.

For the segmentation stage, the mean shape learned previously is initialised in the test image. The same associated texture images as in the training stage are computed. For each landmark l , a neighbourhood of patches are used to sample the texture images and a reconstruction is obtained using the appearance model previously trained. The new landmark location will be defined as the position where the MI is maximal between the reconstructed and original values. This scheme is performed in a multi-resolution manner as in (191).

Subsequently, Viswanath *et al.* in (150), used the weighted ensemble of regional image textures for active shape model segmentation (WERITAS) method also proposed by (193). WERITAS and MANTRA methods, both are based on the ASM formulation. However, they differ in the last stage, where in WERITAS instead of using MI to adapt the positions of new landmarks, a Mahalanobis distance metric is used. In the training stage, the Mahalanobis distance is computed between landmarks and neighbour patches for each of the features. Subsequently, a new metric is proposed as a linear weighted combination of those Mahalanobis distances which maximises the correlation with the Euclidean distance between the patches and the true landmarks. In the segmentation step, this metric is then computed between the initialised landmarks and neighbouring patches in order to update landmark positions, in a similar fashion to other active contour model (ACM) models. [Check the commented senetence in the tex file.](#)

Litjens *et al.* (125) and Vos *et al.* (154) used an approach proposed in (194) in which the bladder, prostate and rectum are segmented. The segmentation task is performed as an optimization problem taking three parameters into account linked to organs such as: (i) the shape (an ellipse), (ii) the location and (iii) the respective angles between them. Furthermore, Litjens *et al.* (125) used only ADC map to encode the appearance whereas Vos *et al.* (154) used both ADC and T_2 maps. Then, during the optimization using a quasi-Newton optimizer, an objective function is minimized. This function is defined as the sum of the deviations from the above model learnt. This rough segmentation is then used inside a Bayesian framework to refine the segmentation.

Only the work of Tiwari *et al.* in (141) propose a segmentation based on MRSI. Authors localized the voxels corresponding to the prostate organ using a hierarchical spectral clustering. First, each MRSI spectrum is projected into a lower dimension space using graph embedding (195). To proceed, a similarity matrix W is computed

3. REVIEW OF CADE AND CADX FOR CAP

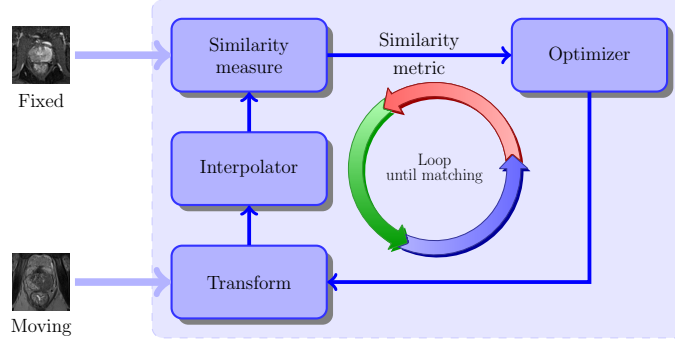


Figure 3.8: Typical framework involved to solve the registration problem.

using a Gaussian similarity measure from Euclidean distance (196)) such that:

$$W(\mathbf{x}, \mathbf{y}) = \begin{cases} \exp\left(\frac{\|s(\mathbf{x}) - s(\mathbf{y})\|_2^2}{\sigma^2}\right) & , \text{ if } \|\mathbf{x} - \mathbf{y}\|_2 < \epsilon , \\ 0 & , \text{ if } \|\mathbf{x} - \mathbf{y}\|_2 > \epsilon . \end{cases} \quad (3.18)$$

where $s(\mathbf{x})$ and $s(\mathbf{y})$ are the MRSI spectra for the voxels \mathbf{x} and \mathbf{y} respectively, σ is the standard deviation of the Gaussian similarity measure and ϵ is the parameter to defined an ϵ -neighbourhood.

The MRSI spectra projection into the lower dimension space is approached as a generalized eigenvector problem. Subsequently, a replicate k-means clustering method is run defining two clusters. The data corresponding to larger cluster is assumed to belong to the non-prostate voxels and these voxels will be eliminated from the processing. The full procedure is repeated until the total number of voxels left is inferior to a given threshold set experimentally.

3.1.3 Registration

The role of image registration is vital in CAD systems using multi-parametric MRI images. As it will be discussed in Sect. 3.2, for the sake of an optimal classification, the features detected in each modality will be grouped depending of their spatial locations. Hence, one has to ensure the perfect alignment of the multi-modal MRI images ahead of performing any classification.

Image registration is the procedure consisting of aligning an unregistered image (also called moving image) into a template image (also called fixed image) via a geometric transformation. This problem is usually addressed as presented in Fig. 3.8. An iterative procedure takes place to infer the geometric transformation (parametric or non-parametric) via an optimizer, which maximizes the similarity between the two images. In the following, a review of the different components of a typical registration framework: transformation model, similarity metric, optimizer and interpolation are presented, followed by a summary of registratio approaches applied in CAD for CaP

systems. Exhaustive reviews covering all registration methods in computer science and medical fields can be found in (197) and (198).

Geometric transformation models: As previously mentioned, the registration problem is to align two images or volumes by finding the geometric transformation. Regarding the transformation, from all CAD systems reviewed, only parametric methods have been implemented. Three different groups of parametric transformation models have been used, rigid, affine, and elastic, each of them are characterized by the degree of freedom that they offer.

The first type of transformation is usually referred to as rigid transformation. These transformations are only composed of rotation and translation transforms. Hence, for a 2D space where $\mathbf{x} = (x, y) \in \mathbb{R}^2$, a rigid transformation \mathcal{T}_R is formalized as as:

$$\begin{aligned}\mathcal{T}_R(\mathbf{x}) &= \begin{bmatrix} R & \mathbf{t} \\ \mathbf{0}^T & 1 \end{bmatrix} \mathbf{x}, \\ &= \begin{bmatrix} \cos \theta & -\sin \theta & t_x \\ \sin \theta & \cos \theta & t_y \\ 0 & 0 & 1 \end{bmatrix} \begin{bmatrix} x \\ y \\ 1 \end{bmatrix},\end{aligned}\quad (3.19)$$

where θ is the rotation angle and $\{t_x, t_y\}$ represents the translation along $\{x, y\}$ respectively.

In the case of 3D registration using volume, an additional component z has to be taken into account such that $\mathbf{x} = (x, y, z)$. Thus, the rotation matrix \mathbf{R} becomes of size 3×3 whereas the translation vector \mathbf{t} consists of a vector of three elements. Hence, the geometric transformation $\mathcal{T}_R(\cdot)$ is embedded into a matrix of size 4×4 .

Affine transformations provide additional degrees of freedom managing rotations and translation as with the rigid transformations but also shearing and scaling. Hence, for a 2D space where $\mathbf{x} = (x, y) \in \mathbb{R}^2$, an affine transformation \mathcal{T}_A is formalized as:

$$\begin{aligned}\mathcal{T}_A(\mathbf{x}) &= \begin{bmatrix} A & \mathbf{t} \\ \mathbf{0}^T & 1 \end{bmatrix} \mathbf{x}, \\ &= \begin{bmatrix} a_{11} & a_{12} & t_x \\ a_{21} & a_{22} & t_y \\ 0 & 0 & 1 \end{bmatrix} \begin{bmatrix} x \\ y \\ 1 \end{bmatrix}.\end{aligned}\quad (3.20)$$

Hence the four parameters $\{a_{11}, a_{12}, a_{21}, a_{22}\}$ of the affine matrix and $\{t_x, t_y\}$ of the translation encode an affine transformation.

Regarding volume registration, the previously mentioned remark can be applied as well. Thus the geometric transformation $\mathcal{T}_A(\cdot)$ is of size 4×4 with nine parameters involved.

Finally, the last group of transformations is known as elastic transformations and offer the advantage to handle local distortions. In the reviewed CAD systems, the radial

3. REVIEW OF CADE AND CADX FOR CAP

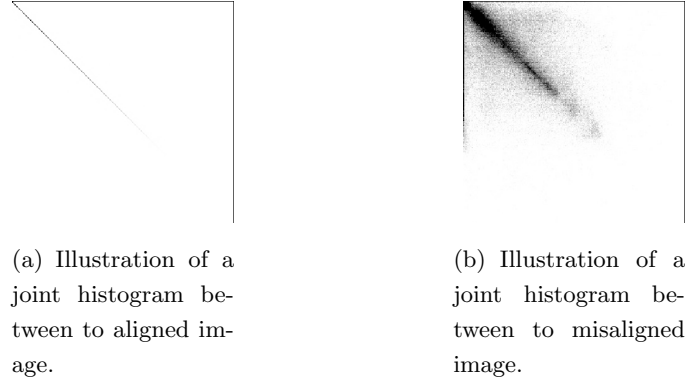


Figure 3.9: Difference observed in joint histogram between aligned and misaligned images. The joint measure will be more concentrated of the histogram in the case that the images are aligned and more randomly distributed in the case that both images are more misaligned.

basis functions are used to formalize the local distortions such as:

$$\mathcal{T}_E(\mathbf{x}) = \frac{a_{11}x - a_{12}y + t_x + \sum_i c_i g(\|\mathbf{x} - p_i\|)}{a_{21}x + a_{22}y + t_y + \sum_i c_i g(\|\mathbf{x} - p_i\|)}, \quad (3.21)$$

where \mathbf{x} are the control points in both images and $g(\dots)$ is the actual radial basis function.

Two radial basis functions are used: (i) the TPS and (ii) the B-splines. Apart from the formalism, these two approaches have a main difference: with B-splines, the control points are usually uniformly and densely placed on a grid where as with TPS, the control points correspond to detected or selected key points. By using TPS, Mitra *et al.* (199) obtained more accurate and time efficient results than with the B-splines strategy (200).

It is reasonable to point out that usually only rigid or affine registrations are used to register multi-parametric images from a same protocol. Elastic registration methods are more commonly used to register multi-protocol images (e.g., histopathology with MRI images) (190, 193).

Similarity measure: The most naive similarity measure used in reviewed registration framework is the mean squared error (MSE) of the SI of MRI images. For a pair of images I and J , the MSE is formalized as:

$$\text{MSE} = \frac{1}{N} \sum_x \sum_y (I(x, y) - J(x, y))^2, \quad (3.22)$$

where N is the total number of pixels. This metric is not well suited when multi-parametric images are involved due to the tissue appearance variations between the different modalities.

In that regard, MI was introduced as a registration measure in the late 1990's by (201). The MI measure finds its foundation in the assumption that a homogeneous region in the first modality image should also appear as a homogeneous region in the second modality even if their SIs are not identical. Thus, those regions share information and the registration task can be achieved by maximizing this common information. Hence, MI of two images A and B is defined as:

$$MI(A; B) = S(A) + S(B) - S(A, B) , \quad (3.23)$$

where $S(A)$ and $S(B)$ are the marginal entropies and $S(A, B)$ is the joint entropy. Then, maximizing the MI is equivalent to minimizing the joint entropy. The joint entropy measure is related with the degree of uncertainty or dispersion of the data in the joint histogram of the images A and B . As shown in Fig. ??, the data in the joint histogram will be concentrated in the case of aligned images while will be more randomly distributed in the case of misaligned images. Regarding the computation of the entropies, an estimation of the PDFs have to be carried out. Histogram or Parzen window methods are a common way to estimate these PDFs.

A generalized form of MI, combined mutual information (CMI), was proposed by (202). CMI encompasses interdependent information such as texture and gradient into the metric. Hence, for both of images A and B , the image ensembles ϵ_n^A and ϵ_m^B are generated and composed of n and m images based on the texture and gradient. Then, the CMI can be formulated such as:

$$CMI(\epsilon_n^A; \epsilon_m^B) = S(\epsilon_n^A) + S(\epsilon_m^B) - S(\epsilon_n^A, \epsilon_m^B) . \quad (3.24)$$

Check the commented text, It is not well written and I did not include them

Optimization methods: Registration is usually regarded as an optimization problem where the parameters of the geometric transformation model have to be inferred by minimizing the similarity measure. Iterative estimation methods are commonly used being the L-BFGS-B quasi-Newton method (203) and gradient descent (204) the most common ones. During our review, we noticed that authors do not usually linger over optimizer choice.

Interpolation: The registration procedure involves transforming an image, and pixels mapped to non-integer points must be approximated using interpolation methods. As for the optimization methods, we notice that little attention has been paid on the choice of those interpolations methods. However, commonly used methods are bilinear, nearest-neighbour, bi-cubic, spline and inverse-distance weighting method (205).

Registration methods used in CAD systems: Studies presenting CAD pipeline incorporating an automatic registration procedure are summarized in Tab. 3.4.

3. REVIEW OF CADE AND CADX FOR CAP

Table 3.4: Classification of the different registration methods used in the CAD systems reviewed. Acronyms: gradient descent (GD), Nelder-Mead (NM).

Study index	Modality registered	Type	Geometric model		Similarity measure			Optimizer	
			Affine	Elastic	MSE	MI	CMI	GD	L-BFGS-B
(116, 117)	T ₂ -W - DCE	2D	✓	—	✓	—	—	—	—
(122)	T ₂ -W - DW	2D	✓	✓	—	—	—	—	—
(122)	T ₂ -W - DCE	2D	✓	✓	—	✓	—	✓	—
(147, 148)	T ₂ -W - DCE	2D	✓	—	—	✓	—	—	—
(149)	T ₂ -W - DCE - DW	3D	✓	—	—	—	✓	✓	—
(151)	T ₂ -W - DCE	3D	✓	—	—	✓	—	—	—
(153)	T ₂ -W - DCE	3D	✓	✓	—	✓	—	—	✓

Notes:

—: not used or not mentioned.

✓: used or implemented.

Ampeliotis *et al.* in (116, 117) did not use the framework as presented in Fig. 3.8 to register 2D T₂-W and DCE images. By using image symmetries and the MSE metric, they find the parameters of an affine transformation but without using a common objective function. They were finding independently and sequentially the scale factor, the rotation and finally the translation.

Giannini *et al.* (122) used also a in-house registration method for 2D T₂-W and DW images using an affine model. The bladder is first segmented in both modalities in order to obtain its contours and to focus the registration.

Giannini *et al.* (122) and also Vos *et al.* (153) used the same framework which is based on finding an affine transformation to register the T₂-W and DCE images using MI (206). Then, an elastic registration using B-spline takes place using the affine parameters to initialize the geometric model with the same similarity measure. However, the approaches differ regarding the choice of the optimizer since a gradient descent is used in (122) and the same optimization problem is tackled via quasi-Newton method in (153). Moreover, Giannini *et al.* (122) performed a 2D registration whereas Vos *et al.* (153) registered 3D volumes.

Viswanath *et al.* in (147, 148) as well as Vos *et al.* (151) performed an affine registration using the MI as similarity measure to correct the misalignment between T₂-W and DCE images. The choice of the optimizer was not specified. Viswanath *et al.* (147, 148) focused on 2D registration while Vos *et al.* (151) performed 3D registration.

Finally, Viswanath *et al.* in (149) performed a 3D registration with the three modalities, T₂-W and DCE and DW MRI, by using an affine transformation model combined with the CMI similarity measure as presented in (202). Moreover, in this latter work, the authors employed gradient descent (202) employed gradient descent approach to solve this problem but suggested Nelder-Mead simplex and quasi-Newton method as other solutions.

Table 3.5: Overview of the CADe strategies employed in CAD systems.

CADe: ROIs selection strategy	References
All voxels-based approach	(119, 120, 122, 123, 128, 130, 132, 133, 134, 135, 136, 138, 139, 140, 141, 142, 143, 144, 145, 146, 147, 148, 149, 150)
Lesions candidate detection	(125, 126, 127, 154)

3.2 Image classification framework

3.2.1 CADe: ROIs detection/selection

As discussed in the introduction and shown in Fig. 2.1, the image classification framework is often composed of a CADe and a CADx. In this section, we will focus on studies embedding a CADe in their framework. Two approaches are considered to define a CADe (see Tab. 3.5): (i) voxel-based delineation and (ii) lesion segmentation. The first strategy, which concerns the majority of the studies reviewed (see Tab. 3.5), is in fact linked to the nature of the classification framework (119, 120, 122, 123, 128, 130, 132, 133, 134, 135, 136, 138, 139, 140, 141, 142, 143, 144, 145, 146, 147, 148, 149, 150). All voxels are considered as a possible lesion and the output of the framework will be pixels classified as lesion and non lesion. The second group of methods is composed of method implementing a lesion segmentation algorithm to delineate potential candidates to further obtain a diagnosis through the CADx. This approach was borrowed from other application areas such as breast cancer. These methods are in fact very similar to the classification framework used in CADx later.

Vos *et al.* (154) highlighted lesion candidates by detecting blobs in the ADC map. These candidates were filtered using some *a priori* criteria such as SI or diameter. As mentioned in Sect. 2.2.6 (see also Tab. 2.1), CaP can be interpreted as region of lower SI in ADC map. Hence, blob detectors are suitable to highlight these regions. Blobs are detected in a multi-resolution scheme, by computing the three main eigenvalues $\{\lambda_{\sigma,1}, \lambda_{\sigma,2}, \lambda_{\sigma,3}\}$ of the Hessian matrix, for each voxel location of the ADC map at a specific scale σ (207). The probability p of a voxel \mathbf{x} being a part of a blob at the scale σ is given by:

$$P(\mathbf{x}, \sigma) = \begin{cases} \frac{\|\lambda_{\sigma,3}(\mathbf{x})\|^2}{\|\lambda_{\sigma,1}(\mathbf{x})\|} , & \text{if } \lambda_{\sigma,k}(\mathbf{x}) > 0 \text{ with } k = \{1, 2, 3\} , \\ 0 , & \text{otherwise .} \end{cases} \quad (3.25)$$

The fusion of the different scales is computed as:

$$L(\mathbf{x}) = \max P(\mathbf{x}, \sigma), \forall \sigma . \quad (3.26)$$

3. REVIEW OF CADE AND CADX FOR CAP

The candidate blobs detected are then filtered depending on its appearance (cf. maximum of the likelihood of the region, diameter of the lesion) and their SI in ADC and T₂-W images. The detected regions are then used as inputs for the CADx.

Litjens *et al.* in (125) used a pattern recognition approach in order to delineate the ROIs. A blobness map was calculated in the same manner as in (153) using the multi-resolution Hessian blob detector on the ADC map, T₂-W and pharmacokinetic parameters maps (see Sect. 3.2.2 for details about those parameters). Additionally, the position of the voxel $\mathbf{x} = \{x, y, z\}$ was used as a feature as well as the Euclidean distance of the voxel to the prostate center. Hence, the feature vectors were composed of eight features and a support vector machines (SVM) classifier was trained using a radial basis function (RBF) kernel (see Sect. ?? for more details).

Subsequently, Litjens *et al.* in (126) modified this approach by including only features related to the blob detection on the different maps as well as the original SIs of the parametric images. Two new maps were introduced based on texture. Instead of a SVM classifier, a k -nearest neighbour (k -NN) classifier was used. The candidate regions were then extracted by performing a local maxima detection followed by post-processing region-growing and morphological operations.

3.2.2 CADx: Feature detection

Discriminative features which can be used to recognize CaP from healthy tissue have to be first detected. This processing is known in computer vision as feature extraction. However, feature extraction is also the name given in pattern recognition to some types of dimension reduction methods which will be presented next. In order to avoid confusion between these two aspects, in this survey, the procedure “detecting” or “extracting” features from images and signals will be defined as feature detection. This section will summarize the different strategies employed for this task. The features used in the studies are summarized in Table. ??.

3.2.2.1 Image-based features

This section will focus on image-based features detection. Two main strategies to detect features have been identified and used for the purpose of our classification: (i) voxel-wise detection and (ii) region-wise detection.

Voxel-wise detection: This strategy refers to the fact that a feature is extracted at each voxel location. CaP as previously discussed (see Tab. 2.1) can be discerned due to SI changes. Hence, intensity-based features are one of the most common features used to build the feature vector which has to be classified (2, 3, 116, 117, 119, 120, 121, 124, 128, 147, 149). This type of feature consists simply of the SI of each voxel of the different MRI modalities.

Edge based features have also been used to detect SI changes. Each feature is computed by convolving the original image with an edge operator. Three of these operators

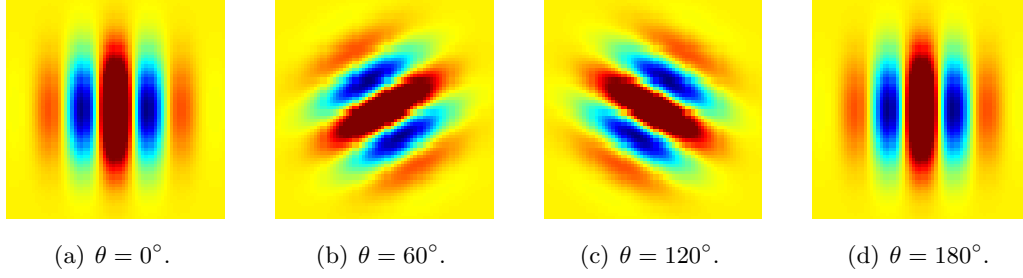


Figure 3.10: Illustration of four different Gabor filters varying their orientations θ .

are used: (i) Prewitt operator (208), (ii) Sobel operator (209) and (iii) Kirsch operator (210). Results obtained with these operators vary, due to their different kernels. These features are commonly incorporated in the feature vector for further classification in the CAD systems reviewed (2, 3, 142, 143, 145, 146, 149).

Gabor filters (211, 212) offer another approach to extract information related to edges and texture and were integrated in three different CAD for CaP (144, 147, 150). A Gabor filter is defined by the modulation of a Gaussian function with a sinusoid which can be further rotated. Hence, a Gabor filter g can be formalized as:

$$g(x, y; \theta, \psi, \sigma, \gamma) = \exp\left(-\frac{x'^2 + \gamma^2 y'^2}{2\sigma^2}\right) \cos\left(2\pi \frac{x'}{\lambda} + \phi\right), \quad (3.27)$$

with

$$\begin{aligned} x' &= s(x \cos \theta + y \sin \theta), \\ y' &= s(-x \sin \theta + y \cos \theta), \end{aligned}$$

where λ is the wavelength of the sinusoidal factor, θ represents the orientation of the Gabor filter, ψ is the phase offset, σ is the standard deviation of the Gaussian envelope, γ is the spatial aspect ratio and s is the scale factor. To perform Gabor analysis to extract features for a classification scheme, a bank of Gabor filters is usually created with different angles, scale and dilatations (see Fig. 3.10) and then convolved with the image.

Texture-based features provide other characteristics discerning CaP from healthy tissue. The most common texture analysis for image classification are co-occurrence matrices with their related statistics which were proposed in (4) and are commonly used in CAD systems (2, 3, 118, 142, 143, 145, 146, 147, 149, 150). At each voxel, a neighbourhood is defined around this center and a gray-level co-occurrence matrix is built by selecting a pair of voxels based on a defined distance and angle. Then, using this co-occurrence matrix, a set of features can be computed based on the statistics describing the texture around each voxel. Computation of these features is presented in Tab. 3.6.

3. REVIEW OF CADE AND CADX FOR CAP

Table 3.6: The fourteen statistical features for texture analysis commonly computed from the gray level co-occurrence matrix p as presented by (4).

Statistical features	Formula
Angular second moment	$\sum_i \sum_j p(i, j)^2$.
Contrast	$\sum_{n=0}^{N_g-1} n^2 \{ \sum_{i=1}^{N_g-1} \sum_{j=1}^{N_g-1} p(i, j) \} , i - j = n$.
Correlation	$\frac{\sum_i \sum_j (ij) p(i, j) - \mu_x \mu_y}{\sigma_x \sigma_y}$.
Variance	$\sum_i \sum_j (i - \mu)^2 p(i, j)$.
Inverse difference moment	$\sum_i \sum_j \frac{1}{1 + (i - \mu)^2} p(i, j)$.
Sum average	$\sum_{i=2}^{2N_g} i p_{x+y}(i)$.
Sum variance	$\sum_{i=2}^{2N_g} (i - f_s)^2 p_{x+y}(i)$.
Sum entropy	$-\sum_{i=2}^{2N_g} p_{x+y}(i) \log p_{x+y}(i)$.
Entropy	$-\sum_i \sum_j p(i, j) \log p(i, j)$.
Difference variance	$\sum_{i=0}^{N_g-1} i^2 p_{x-y}(i)$.
Difference entropy	$-\sum_{i=0}^{N_g-1} p_{x-y}(i) \log p_{x-y}(i)$.
Info. measure of corr. 1	$\frac{S(X;Y) - S_1(X;Y)}{\max(S(X), S(Y))}$.
Info. measure of corr. 2	$\sqrt{(1 - \exp[-2(H_2(X;Y) - H(X;Y))])}$.
Max. corr. coeff.	$\sqrt{\lambda_2}$, of $Q(i, j) = \sum_k \frac{p(i, k)p(j, k)}{p_x(i)p_y(k)}$.

Fractal analysis and more precisely a local estimation of the fractal dimension (213) describing the texture roughness at a specific location was used in (130). A wavelet-based method in a multi-resolution framework was used to estimate the fractal dimension. Cancerous tissue were characterized to have a higher fractal dimension than healthy tissue.

Chan *et al.* (121) described the texture using the frequency signature via the discrete cosine transform (DCT) (214)) defining a neighbourhood of 7×7 pixels for each of the modalities that they used. The DCT allows to decompose a portion of image into a coefficients space where few of these coefficients encoded the visually significant information. The DCT coefficients are computed such as:

$$C_{k_1, k_2} = \sum_{m=0}^{M-1} \sum_{n=0}^{N-1} p_{m,n} \cos \left[\frac{\pi}{M} \left(m + \frac{1}{2} \right) k_1 \right] \cos \left[\frac{\pi}{N} \left(n + \frac{1}{2} \right) k_2 \right], \quad (3.28)$$

where C_{k_1, k_2} is the DCT coefficient at the position k_1, k_2 , M and N are the dimension of the neighbourhood and $p_{m,n}$ is the pixel SI at the position $p_{m,n}$.

Viswanath *et al.* (150) projected T₂-W images into the wavelet space, using Haar wavelet, and used the coefficients obtained from the decomposition as features.

Finally Litjens *et al.* in (125) computed the texture map based on T₂-W images using a Gaussian filter bank.

Region-wise detection: Unlike the previous section, another strategy is to study an entire region and extract characteristic features corresponding to this region. The most common approach reviewed can be classified as statical methods. First a feature map is computed for the whole image instead of using single voxels. Then, ROIs are defined and statistics are extracted from each of these regions. The most widely used statistics is based on percentiles and is widely used (78, 118, 125, 126, 142, 143, 145, 146, 147, 149, 150, 151, 152, 153, 154). The percentile used is usually manually determined observing the distribution and corresponds to the best discriminant value differentiating malignant and healthy tissue. In addition, statistic-moments such as mean, standard deviation, kurtosis and skewness are also used (2, 3, 78, 116, 117, 118). Litjens *et al.* in (?) also introduced a feature based on symmetry. They compute the mean of a candidate lesion as well as its mirrored counter-part and compute the quotient as feature.

Another subset of features are anatomic which were also used in (126, 132). Litjens *et al.* in (??) computed the volume, compactness and sphericity related to the region to integrate it in their feature vector. Matulewicz *et al.* (132) introduced four features corresponding to the percentage of tissue belonging to the regions PZ, CG, periurethral region or outside prostate region for the considered ROI.

In contrast to anatomical are histogram-based features. For instance, Liu *et al.* (129) introduced four different types of histogram-based features. The first type corresponds to the histogram of the SI of the image. The second type is the histogram of oriented gradient (HOG) (215). HOG descriptor describes the local shape of the object of interest

3. REVIEW OF CADE AND CADX FOR CAP

by using distribution of gradient directions. This descriptor is extracted mainly in three steps. First the gradient image and its corresponding magnitude and direction are computed. Then, the ROI is divided into cells and an oriented-based histogram is generated for each cell. At each pixel location, the orientation of the gradient will vote for a bin of the histogram and this vote is weighted by the magnitude of the same gradient. Finally, The cells are grouped into block and each block is normalized. The third histogram-based type used in (129) was shape context (216). The shape context is also a way to describe the shape of an object of interest. First, a set of points defining edges have to be detected and for each point of each edge, a log-polar-based histogram is computed using the relative points distribution. The last set of histogram-based feature extracted is based on the framework described in (217) which is using the Fourier transform of the histogram created via local binary pattern (LBP) (186). LBP is generated by comparing the value of the central pixel with its 8-connected neighbours. Then, in the ROI, the histogram of the LBP distribution is computed. The discrete fourier transform (DFT) of the LBP histogram is used to make the feature invariant to rotation.

The last group of region-based feature is based on fractal analysis. The features proposed are based on estimating the fractal dimension which is a statistical index representing the complexity of what is analysed. Lv *et al.*, (131) proposed two features based on fractal dimension: (i) texture fractal dimension and (ii) histogram fractal dimension. The first feature is based on estimating the fractal dimension on the SI of each image. Hence, this feature is a statistical characteristic of the image roughness. The second fractal dimension is estimated in the PDF of each image and characterises the complexity of the PDF. Lopes *et al.* (130) proposed a 3D version to estimate the fractal dimension of a volume using wavelet decomposition.

3.2.2.2 DCE-based features

DCE-MRI is more commonly based on a SI analysis over time as presented in Sect. 2.2.3. In this section the features extracted for DCE-MRI analysis are presented.

Whole-spectra approach: Some studies are using the whole DCE time series as feature vector (116, 117, 144, 146, 147). In some cases, the high-dimensional feature space is reduced using dimension reduction methods as it will be presented in the next section (see Sect. 3.2.3).

Semi-quantitative approach: Semi-quantitative approaches are based on mathematically modelling the DCE time series. The parameters modelling the signal are commonly used, mainly due to the simplicity of their computation. Parameters included in semi-quantitative analysis are summarized in Tab. 3.7 and also graphically depicted in Fig. 3.11. A set of time features corresponding to specific amplitude level (start, maximum and end) are extracted. Then, derivative and integral features are also considered as discriminative and are commonly computed.

Table 3.7: Parameters used as features for a DCE semi-quantitative analysis in CAD systems.

Semi-quantitative features	Explanations
<i>Amplitude features:</i>	
S_0	Amplitude at the onset of the enhancement
S_{\max}	Amplitude corresponding to 95% of the maximum amplitude
S_p	Amplitude corresponding to the maximum amplitude
S_f	Amplitude at the final time point
<i>Time features:</i>	
t_0	Time at the onset of the enhancement
t_{\max}	Time corresponding to 95% of the maximum amplitude
t_p	Time corresponding to the maximum amplitude
t_f	Final time
t_{tp}	Time to peak which is the time from t_0 to t_p
<i>Derivatives and integral features:</i>	
WI	Wash-in rate corresponding to the signal slope from t_0 to t_m or t_p
WO	Wash-out rate corresponding to the signal slope from t_m or t_p to t_p
$IAUC$	Initial area under the curve which is the area between t_0 to t_f

3. REVIEW OF CADE AND CADX FOR CAP

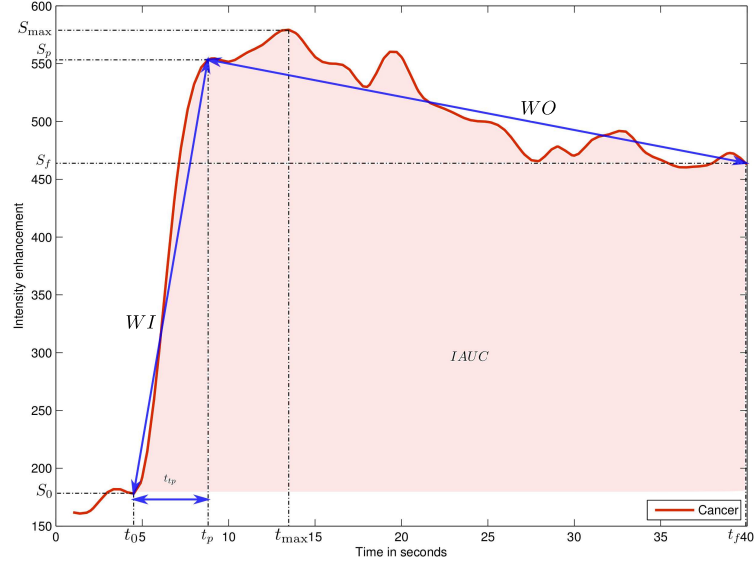


Figure 3.11: Graphical representation of the different semi-quantitative features used for DCE-MRI analysis.

Quantitative approach: As presented in Sect. 2.2, quantitative approaches correspond to mathematical-pharmacokinetic models based on physiological exchanges. Four different models have been used in CAD for CaP systems. The most common model reviewed was the *Brix model* (119, 120, 128, 134, 135, 138). This model is formalized such as:

$$\frac{S(t)}{S(0)} = 1 + Ak_{ep} \left(\frac{\exp(-k_{ep}t) - \exp(-k_{el}t)}{k_{el} - k_{ep}} \right), \quad (3.29)$$

where $S(\cdot)$ is the DCE signal, A is the parameter simulating the tissue properties, k_{el} is the parameter related to the first-order elimination from the plasma compartment and k_{ep} is the parameter of the transvascular permeability. These parameters (k_{ep} , k_{el} , A) are computed from the MRI data and used as features.

Another model is Tofts model (95) which was used in (2, 3, 122, 124, 133). In this model, the DCE signal relative to the concentration is presented as:

$$C_t(t) = v_p C_p(t) + K_{trans} \int_0^t C_p(\tau) \exp(-k_{ep}(t - \tau)) d\tau, \quad (3.30)$$

where $C_t(\cdot)$ is the concentration of the medium, $C_p(\cdot)$ is the AIF which have to be estimated independently, K_{trans} is the parameter related to the diffuse transport of media across the capillary endothelium, k_{ep} is the parameter related to the exchanges back into the vascular space and v_e is the extravascular-extracellular space fraction defined such

that $v_e = 1 - v_p$. In this model, parameters K_{trans} , k_{ep} and v_e are computed and used as features.

Mazzetti *et al.* (133) and Giannini *et al.* (122) used the Weibull function in different empirical model based on West-like function and referred to as the phenomenological universalities model (218) defined by three parameters β , a_0 , and r (see Eq. 3.31).

$$S(t) = \exp \left[rt + \frac{1}{\beta} a_0 - r (\exp(\beta t) - 1) \right] , \quad (3.31)$$

For all these models, the parameters are inferred using an optimization curve fitting approach.

3.2.2.3 MRSI-based features

Whole spectra approach: As in the case of DCE analysis, one common approach is to incorporate the whole MRSI spectra in the feature vector for classification (123, 132, 136, 139, 141, 142, 143, 145, 147). Sometimes post-processing involving dimension reduction methods is performed to reduce the complexity during the classification as it will be presented in Sect. 3.2.3.

Quantification approach: We can reiterate that in MRSI only few biological markers (cf., choline, creatine and citrate metabolites mainly) are known to be useful to discriminate CaP and healthy tissue. Then, concentrations of these metabolites can be considered as a feature used for classification. In order to perform this quantification, four different approaches have been used. The QUEST (219), AMARES (220) and VARPRO (221) models were used in (123). They are all time-domain quantification methods varying by the type of pre-knowledge embedded and the optimization approaches used to solve the quantification problem. Unlike the time-domain quantification approaches, Parfait *et al.* (136) used the LcModel approach (222) which solves the optimization problem in the frequency domain.

Although Parfait *et al.* (136) used each metabolite concentration individually, other authors such as Kelm *et al.* (123) proposed to compute relative concentrations as the ratio of the choline plus creatine to citrate (see Eq. (3.32)) or the ratio of citrate to choline plus creatine plus citrate (see Eq. (3.33)).

$$R_1 = \frac{[\text{Cho}] + [\text{Cr}]}{[\text{Cit}]} . \quad (3.32)$$

$$R_2 = \frac{[\text{Cit}]}{[\text{Cho}] + [\text{Cr}] + [\text{Cit}]} , \quad (3.33)$$

where Cit, Cho and Cr are the concentration of citrate, choline and creatine respectively.

Wavelet decomposition approach: Tiwari *et al.* (144) performed a wavelet packet decomposition (223) of the spectra with the Haar wavelet basis function and used its coefficients as features.

3. REVIEW OF CADE AND CADX FOR CAP

3.2.3 CADx: Feature selection and feature extraction

References

- [1] L. G. NYUL, J. K. UDUPA, AND X. ZHANG. **New variants of a method of MRI scale standardization.** *IEEE Trans Med Imaging*, **19**(2):143–150, Feb 2000. ix, 29, 30
- [2] E. NIAF, O. ROUVIERE, AND C. LARTIZIEN. **Computer-aided diagnosis for prostate cancer detection in the peripheral zone via multisequence MRI.** In *Proc. SPIE 7963, Medical Imaging 2011: Computer-Aided Diagnosis*, 2011. ix, 23, 30, 31, 35, 36, 44, 45, 47, 50
- [3] E. NIAF, O. ROUVIERE, F. MEGE-LECHEVALLIER, F. BRATAN, AND C. LARTIZIEN. **Computer-aided diagnosis of prostate cancer in the peripheral zone using multiparametric MRI.** *Phys Med Biol*, **57**(12):3833–3851, Jun 2012. ix, 23, 30, 31, 35, 36, 44, 45, 47, 50
- [4] R.M. HARALICK, K. SHANMUGAM, AND ITS'HAK DINSTEN. **Textural features for image classification.** *Systems, Man and Cybernetics, IEEE Transactions on*, **SMC-3**(6):610–621, 1973. xi, 45, 46
- [5] Y. J. CHOI, J. K. KIM, N. KIM, K. W. KIM, E. K. CHOI, AND K. S. CHO. **Functional MR imaging of prostate cancer.** *Radiographics*, **27**:63–75, 2007. 2, 12, 14, 15, 16, 19
- [6] K. H. LEISSNER AND L. E. TISELL. **The weight of the human prostate.** *Scand. J. Urol. Nephrol.*, **13**(2):137–142, 1979. 1
- [7] S. PARFAIT. *Classification de spectres et recherche de biomarqueurs en spectroscopie par résonance magnétique nucléaire du proton dans les tumeurs prostatiques.* PhD thesis, Université de Bourgogne, 2010. 1, 3, 4, 18
- [8] J. E. MCNEAL. **The zonal anatomy of the prostate.** *Prostate*, **2**:35–49, 1981. 1
- [9] H. HRICAK, G. C. DOOMS, J. E. MCNEAL, A. S. MARK, M. MAROTTI, A. AVALLONE, M. PELZER, E. C. PROCTOR, AND E. A. TANAGHO. **MR imaging of the prostate gland: normal anatomy.** *AJR Am J Roentgenol*, **148**:51–58, Jan 1987. 2, 8, 9
- [10] A. VILLERS, A. STEG, AND L. BOCCON-GIBOD. **Anatomy of the prostate: review of the different models.** *Eur. Urol.*, **20**:261–268, 1991. 2
- [11] F. V. COAKLEY AND H. HRICAK. **Radiologic anatomy of the prostate gland: a clinical approach.** *Radiol. Clin. North Am.*, **38**:15–30, Jan 2000. 2
- [12] J. FERLAY, H. R. SHIN, F. BRAY, D. FORMAN, C. MATHERS, AND D. M. PARKIN. **Estimates of worldwide burden of cancer in 2008: GLOBOCAN 2008.** *Int. J. Cancer*, **127**(12):2893–2917, Dec 2010. 2
- [13] R. SIEGEL, D. NAISHADHAM, AND A. JEMAL. **Cancer statistics, 2013.** *CA Cancer J Clin*, **63**(1):11–30, Jan 2013. 3
- [14] A. C. AMERICAN CANCER SOCIETY. **Cancer Facts and Figures 2013.** <http://www.cancer.org/research/cancerfactsfigures>, 2013. Accessed: 2013-08-01. 3
- [15] A. C. AMERICAN CANCER SOCIETY. **Cancer Facts and Figures 2010.** <http://www.cancer.org/research/cancerfactsfigures>, 2010. Accessed: 2013-08-01. 3
- [16] E. GIOVANNUCCI, Y. LIU, E. A. PLATZ, M. J. STAMPFER, AND W. C. WILLETT. **Risk factors for prostate cancer incidence and progression in the health professionals follow-up study.** *Int. J. Cancer*, **121**(7):1571–1578, Oct 2007. 3
- [17] G. D. STEINBERG, B. S. CARTER, T. H. BEATY, B. CHILDS, AND P. C. WALSH. **Family history and the risk of prostate cancer.** *Prostate*, **17**(4):337–347, 1990. 3
- [18] M. L. FREEDMAN, C. A. HAIMAN, N. PATTERSON, G. J. McDONALD, A. TANDON, A. WALISZEWSKA, K. PENNEY, R. G. STEEN, K. ARDLIE, E. M. JOHN, I. OAKLEY-GIRVAN, A. S. WHITTEMORE, K. A. COONEY, S. A. INGLES, D. ALTSHULER, B. E. HENDERSON, AND D. REICH. **Admixture mapping identifies 8q24 as a prostate cancer risk locus in African-American men.** *Proc. Natl. Acad. Sci. U.S.A.*, **103**(38):14068–14073, Sep 2006. 3
- [19] L. T. AMUNDADOTTIR, P. SULEM, J. GUDMUNDSSON, A. HELGASON, A. BAKER, B. A. AGNARSSON, A. SIGURDSSON, K. R. BENEDIKTSDDOTTIR, J. B. CAZIER, J. SAINZ, M. JAKOBSDDOTTIR, J. KOSTIC, D. N. MAGNUSDDOTTIR, S. GHOSH, K. AGNARSSON, B. BIRGISDDOTTIR, L. LE ROUX, A. OLAFSDOTTIR, T. BLONDAL, M. ANDRESDDOTTIR, O. S. GRETARSDOTTIR, J. T. BERGTHORSSON, D. GUDBJARTSSON, A. GYLFASSON, G. THORLEIFSSON, A. MANOLESCU, K. KRISTJANSSON, G. GEIRSSON, H. ISAKSSON, J. DOUGLAS, J. E. JOHANSSON, K. BALTER, F. WIKLUND, J. E. MONTIE, X. YU, B. K. SUAREZ, C. OBER, K. A. COONEY, H. GRONBERG, W. J. CATALONA, G. V. EINARSSON, R. B. BARKARDOTTIR, J. R. GULCHER, A. KONG, U. THORSTEINSDOTTIR, AND K. STEFANSSON. **A common variant associated with prostate cancer in European and African populations.** *Nat. Genet.*, **38**(6):652–658, Jun 2006. 3
- [20] I. AGALLIU, R. GERN, S. LEANZA, AND R. D. BURK. **Associations of high-grade prostate cancer with BRCA1 and BRCA2 founder mutations.** *Clin. Cancer Res.*, **15**(3):1112–1120, Feb 2009. 3
- [21] R. M. HOFFMAN, F. D. GILLILAND, J. W. ELEY, L. C. HARRIS, R. A. STEPHENSON, J. L. STANFORD, P. C. ALBERTSON, A. S. HAMILTON, W. C. HUNT, AND A. L. POTOSKY. **Racial and ethnic differences in advanced-stage prostate cancer: the Prostate Cancer Outcomes Study.** *J. Natl. Cancer Inst.*, **93**(5):388–395, Mar 2001. 3
- [22] R. W. MA AND K. CHAPMAN. **A systematic review of the effect of diet in prostate cancer prevention and treatment.** *J Hum Nutr Diet*, **22**(3):187–199, Jun 2009. 3

REFERENCES

- [23] D. D. ALEXANDER, P. J. MINK, C. A. CUSHING, AND B. SCEURMAN. **A review and meta-analysis of prospective studies of red and processed meat intake and prostate cancer.** *Nutr J*, **9**:50, 2010. 3
- [24] C. RODRIGUEZ, S. J. FREEDLAND, A. DEKA, E. J. JACOBS, M. L. MCCULLOUGH, A. V. PATEL, M. J. THUN, AND E. E. CALLE. **Body mass index, weight change, and risk of prostate cancer in the Cancer Prevention Study II Nutrition Cohort.** *Cancer Epidemiol. Biomarkers Prev.*, **16**(1):63–69, Jan 2007. 3
- [25] S.B. STRUM AND D. POGLIANO. **What every doctor who treats male patients should know.** PCRI Insights vol. 8, no. 2, May 2005. 3
- [26] G. L. LU-YAO, P. C. ALBERTSEN, D. F. MOORE, W. SHIH, Y. LIN, R. S. DiPAOLA, M. J. BARRY, A. ZIETMAN, M. O’LEARY, E. WALKER-CORKERY, AND S. L. YAO. **Outcomes of localized prostate cancer following conservative management.** *JAMA*, **302**(11):1202–1209, Sep 2009. 3
- [27] G. OSTER, L. LAMERATO, A. G. GLASS, K. E. RICHERT-BOE, A. LOPEZ, K. CHUNG, A. RICHARIYA, T. DODGE, G. G. WOLFF, A. BALAKUMARAN, AND J. EDELSBERG. **Natural history of skeletal-related events in patients with breast, lung, or prostate cancer and metastases to bone: a 15-year study in two large US health systems.** *Support Care Cancer*, **21**(12):3279–3286, Dec 2013. 3
- [28] L. YE, H. G. KYNASTON, AND W. G. JIANG. **Bone metastasis in prostate cancer: molecular and cellular mechanisms (Review).** *Int. J. Mol. Med.*, **20**(1):103–111, Jul 2007. 3
- [29] C. L. CARROL, F. G. SOMMER, J. E. MCNEAL, AND T. A. STAMEY. **The abnormal prostate: MR imaging at 1.5 T with histopathologic correlation.** *Radiology*, **163**(2):521–525, May 1987. 3
- [30] J. E. MCNEAL, E. A. REDWINE, F. S. FREIHA, AND T. A. STAMEY. **Zonal distribution of prostatic adenocarcinoma. Correlation with histologic pattern and direction of spread.** *Am. J. Surg. Pathol.*, **12**(12):897–906, Dec 1988. 3
- [31] T. A. STAMEY, A. N. DONALDSON, C. E. YEMOTO, J. E. MCNEAL, S. SOZEN, AND H. GILL. **Histological and clinical findings in 896 consecutive prostates treated only with radical retropubic prostatectomy: epidemiologic significance of annual changes.** *J. Urol.*, **160**(6 Pt 2):2412–2417, Dec 1998. 3
- [32] R. J. COHEN, B. A. SHANNON, M. PHILLIPS, R. E. MOORIN, T. M. WHEELER, AND K. L. GARRETT. **Central zone carcinoma of the prostate gland: a distinct tumor type with poor prognostic features.** *J. Urol.*, **179**(5):1762–1767, May 2008. 3
- [33] R. ETZIONI, D. F. PENSON, J. M. LEGLER, D. DI TOMMASO, R. BOER, P. H. GANN, AND E. J. FEUER. **Overdiagnosis due to prostate-specific antigen screening: lessons from U.S. prostate cancer incidence trends.** *J. Natl. Cancer Inst.*, **94**(13):981–990, Jul 2002. 3
- [34] C. M. HOEKS, J. O. BARENTSZ, T. HAMBROCK, D. YAKAR, D. M. SOMFORD, S. W. HELJMINK, T. W. SCHEENEN, P. C. VOS, H. HUISMAN, I. M. VAN OORT, J. A. WITJES, A. HEERSCHAP, AND J. J. FUTTERER. **Prostate cancer: multiparametric MR imaging for detection, localization, and staging.** *Radiology*, **261**(1):46–66, Oct 2011. 3, 4, 9, 12, 13, 14, 18
- [35] J. O. BARENTSZ, J. RICHENBERG, R. CLEMENTS, P. CHOYKE, S. VERMA, G. VILLEIRS, O. ROUVIERE, V. LOGAGER, AND J. J. FUTTERER. **ESUR prostate MR guidelines 2012.** *Eur Radiol*, **22**(4):746–757, Apr 2012. 4, 8, 9, 15, 16, 19
- [36] D. F. GLEASON. *Urologic pathology: The prostate*, chapter The Veteran’s Administration Cooperative Urologic Research Group: histologic grading and clinical staging of prostatic carcinoma, page 171198. Lea and Febiger., 1977. 4
- [37] J. I. EPSTEIN, W. C. ALLSBROOK, M. B. AMIN, AND L. L. EGEVAD. **The 2005 International Society of Urological Pathology (ISUP) Consensus Conference on Gleason Grading of Prostatic Carcinoma.** *Am. J. Surg. Pathol.*, **29**(9):1228–1242, Sep 2005. 4
- [38] N. HARA, M. OKUIZUMI, H. KOIKE, M. KAWAGUCHI, AND V. BILIM. **Dynamic contrast-enhanced magnetic resonance imaging (DCE-MRI) is a useful modality for the precise detection and staging of early prostate cancer.** *Prostate*, **62**(2):140–147, Feb 2005. 4
- [39] R. CHOU, J. M. CROSWELL, T. DANA, C. BOGATSOS, I. BLAZINA, R. FU, K. GLEITSMANN, H. C. KOENIG, C. LAM, A. MALTZ, J. B. RUGGE, AND K. LIN. **Screening for prostate cancer: a review of the evidence for the U.S. Preventive Services Task Force.** *Ann. Intern. Med.*, **155**(11):762–771, Dec 2011. 4
- [40] GERALD L. ANDRIOLE, E. DAVID CRAWFORD, ROBERT L. GRUBB, SAUNDRA S. BUYS, DAVID CHIA, TIMOTHY R. CHURCH, MONA N. FOUAD, EDWARD P. GELMANN, PAUL A. KVALE, DOUGLAS J. REDING, JOEL L. WEISSFELD, LANCE A. YOKOCHI, BARBARA O’BRIEN, JONATHAN D. CLAPP, JOSHUA M. RATHMELL, THOMAS L. RILEY, RICHARD B. HAYES, BARNETT S. KRAMER, GRANT IZMIRLIAN, ANTHONY B. MILLER, PAUL F. PINSKY, PHILIP C. PROROK, JOHN K. GOHAGAN, AND CHRISTINE D. BERG. **Mortality results from a randomized Prostate-cancer screening trial.** *New England Journal of Medicine*, **360**(13):1310–1319, 2009. 4
- [41] FRITZ H. SCHRÖDER, JONAS HUGOSSON, MONIQUE J. ROOBOL, TEUVO L.J. TAMMELA, STEFANO CIATTO, VERA NELEN, MACIEJ KWIATKOWSKI, MARCOS LUJAN, HANS LILJA, MARCO ZAPPA, LOUIS J. DENIS, FRANZ RECKER, ALVARO PEZ, LIISA MÄÄTTÄNEN, CHRIS H. BANGMA, GUNNAR AUS, SIGRID CARLSSON, ARNAULD VILLERS, XAVIER REBILLARD, THEODORUS VAN DER KWAST, PAULA M. KUJALA, BERT G. BLIJENBERG, ULF-HAKAN STENMAN, ANDREAS HUBER, KIMMO TAARI, MATTI HAKAMA, SUE M. MOSS, HARRY J. DE KONING, AND ANSSI AUVINEN. **Prostate-cancer mortality at 11 years of follow-up.** *New England Journal of Medicine*, **366**(11):981–990, 2012. 4
- [42] J. HUGOSSON, S. CARLSSON, G. AUS, S. BERGDAHL, A. KHATAMI, P. LODDING, C. G. PIHL, J. STRANNE, E. HOLMBERG, AND H. LILJA. **Mortality results from the Göteborg randomised population-based prostate-cancer screening trial.** *Lancet Oncol.*, **11**(8):725–732, Aug 2010. 4
- [43] A. HEIDENREICH, P. A. ABRAHAMSSON, W. ARTIBANI, J. CATTO, F. MONTORSI, H. VAN POPPEL, M. WIRTH, AND N. MOTTET. **Early detection of prostate cancer: European Association of Urology recommendation.** *Eur. Urol.*, **64**(3):347–354, Sep 2013. 4

- [44] F. H. SCHRODER, H. B. CARTER, T. WOLTERS, R. C. VAN DEN BERGH, C. GOSSELAAR, C. H. BANGMA, AND M. J. ROOBOL. **Early detection of prostate cancer in 2007. Part 1: PSA and PSA kinetics.** *Eur. Urol.*, **53**(3):468–477, Mar 2008. 4
- [45] C. DELPIERRE, S. LAMY, M. KELLY-IRVING, F. MOLINIE, M. VELTEN, B. TRETARRE, A. S. WORONOFF, A. BUEMI, B. LAPOTRE-LEDOUX, S. BARA, A. V. GUIZARD, M. COLONNA, AND P. GROSCLAUDE. **Life expectancy estimates as a key factor in over-treatment: the case of prostate cancer.** *Cancer Epidemiol*, **37**(4):462–468, Aug 2013. 4
- [46] A. BOURDOUMIS, A. G. PAPATSORIS, M. CHRISOFOU, E. EFSATHIOU, A. SKOLARIKOS, AND C. DELIVELIOTIS. **The novel prostate cancer antigen 3 (PCA3) biomarker.** *Int Braz J Urol*, **36**(6):665–668, 2010. 4
- [47] R. MORGAN, A. BOXALL, A. BHATT, M. BAILEY, R. HINDLEY, S. LANGLEY, H. C. WHITAKER, D. E. NEAL, M. ISMAIL, H. WHITAKER, N. ANNELS, A. MICHAEL, AND H. PANDHA. **Engrailed-2 (EN2): a tumor specific urinary biomarker for the early diagnosis of prostate cancer.** *Clin. Cancer Res.*, **17**(5):1090–1098, Mar 2011. 4
- [48] J. CHAD BRENNER, ARULM. CHINNAIYAN, AND SCOTTA. TOMLINS. **ETS fusion genes in prostate cancer.** In DONALD J. TINDALL, editor, *Prostate Cancer*, **16** of *Protein Reviews*, pages 139–183. Springer New York, 2013. 4
- [49] C. M. MOORE, A. RIDOUT, AND M. EMBERTON. **The role of MRI in active surveillance of prostate cancer.** *Curr Opin Urol*, **23**(3):261–267, May 2013. 4
- [50] M. NOGUCHI, T. A. STAMEY, J. E. MCNEAL, AND C. M. YEMOTO. **Relationship between systematic biopsies and histological features of 222 radical prostatectomy specimens: lack of prediction of tumor significance for men with nonpalpable prostate cancer.** *J. Urol.*, **166**(1):104–109, Jul 2001. 5
- [51] G. P. HAAS, N. B. DELONGCHAMPS, R. F. JONES, V. CHANDAN, A. M. SERIO, A. J. VICKERS, M. JUMBELIC, G. THREATTE, R. KORETS, H. LILJA, AND G. DE LA ROZA. **Needle biopsies on autopsy prostates: sensitivity of cancer detection based on true prevalence.** *J. Natl. Cancer Inst.*, **99**(19):1484–1489, Oct 2007. 5
- [52] A. V. TAIRA, G. S. MERRICK, R. W. GALBREATH, H. ANDREINI, W. TAUBENSLAG, R. CURTIS, W. M. BUTLER, E. ADAMOVICH, AND K. E. WALLNER. **Performance of transperineal template-guided mapping biopsy in detecting prostate cancer in the initial and repeat biopsy setting.** *Prostate Cancer Prostatic Dis.*, **13**(1):71–77, Mar 2010. 5
- [53] N. B. DELONGCHAMPS, M. PEYROMAURE, A. SCHULL, F. BEUVON, N. BOUAZZA, T. FLAM, M. ZERBIB, N. MURADYAN, P. LEGMAN, AND F. CORNUD. **Prebiopsy magnetic resonance imaging and prostate cancer detection: comparison of random and targeted biopsies.** *J. Urol.*, **189**(2):493–499, Feb 2013. 5
- [54] M. L. GIGER, H. P. CHAN, AND J. BOONE. **Anniversary paper: History and status of CAD and quantitative image analysis: the role of Medical Physics and AAPM.** *Med Phys*, **35**(12):5799–5820, Dec 2008. 5, 21
- [55] T. HAMBROCK, P. C. VOS, C. A. HULSBERGEN-VAN DE KAA, J. O. BARENTSZ, AND H. J. HUISMAN. **Prostate cancer: computer-aided diagnosis with multiparametric 3-T MR imaging—effect on observer performance.** *Radiology*, **266**(2):521–530, Feb 2013. 5, 6
- [56] H. P. CHAN, B. SAHNER, M. A. HELVIE, N. PETRICK, M. A. ROUBIDOUX, T. E. WILSON, D. D. ADLER, C. PARAMAGUL, J. S. NEWMAN, AND S. SANJAY-GOPAL. **Improvement of radiologists’ characterization of mammographic masses by using computer-aided diagnosis: an ROC study.** *Radiology*, **212**(3):817–827, Sep 1999. 6
- [57] J. C. DEAN AND C. C. ILVENTO. **Improved cancer detection using computer-aided detection with diagnostic and screening mammography: prospective study of 104 cancers.** *AJR Am J Roentgenol*, **187**(1):20–28, Jul 2006. 6
- [58] F. LI, M. AOYAMA, J. SHIRAIISHI, H. ABE, Q. LI, K. SUZUKI, R. ENGELMANN, S. SONE, H. MACMAHON, AND K. DOI. **Radiologists’ performance for differentiating benign from malignant lung nodules on high-resolution CT using computer-estimated likelihood of malignancy.** *AJR Am J Roentgenol*, **183**(5):1209–1215, Nov 2004. 6
- [59] N. PETRICK, M. HAIDER, R. M. SUMMERS, S. C. YESHWANT, L. BROWN, E. M. IULIANO, A. LOUIE, J. R. CHOI, AND P. J. PICKHARDT. **CT colonography with computer-aided detection as a second reader: observer performance study.** *Radiology*, **246**(1):148–156, Jan 2008. 6
- [60] J. V. HEGDE, R. V. MULKERN, L. P. PANYCH, F. M. FENNESSY, A. FEDOROV, S. E. MAIER, AND C. M. TEMPANY. **Multiparametric MRI of prostate cancer: an update on state-of-the-art techniques and their performance in detecting and localizing prostate cancer.** *J Magn Reson Imaging*, **37**(5):1035–1054, May 2013. 6, 9
- [61] H. HRICAK, R. D. WILLIAMS, D. B. SPRING, K. L. MOON, M. W. HEDGCOCK, R. A. WATSON, AND L. E. CROOKS. **Anatomy and pathology of the male pelvis by magnetic resonance imaging.** *AJR Am J Roentgenol*, **141**(6):1101–1110, Dec 1983. 6, 8, 9
- [62] R. A. HUCH BONI, J. A. BONER, U. M. LUTOLF, F. TRINKLER, D. M. PESTALOZZI, AND G. P. KRESTIN. **Contrast-enhanced endorectal coil MRI in local staging of prostate carcinoma.** *J Comput Assist Tomogr*, **19**(2):232–237, 1995. 6
- [63] J. KURHANOWICZ, D. B. VIGNERON, H. HRICAK, P. NARAYAN, P. CARROLL, AND S. J. NELSON. **Three-dimensional H-1 MR spectroscopic imaging of the in situ human prostate with high (0.24-0.7-cm³) spatial resolution.** *Radiology*, **198**(3):795–805, Mar 1996. 6
- [64] J. SCHEIDLER, R. PETSCH, U. MULLER-LISSE, A.F. HEUCK, AND M. REISER. **Echo-planar diffusion-weighted MR imaging of the prostate.** In *Proceedings of the 7th Annual Meeting of ISMRM Philadelphia*, page 1103, 1999. 6, 9, 14
- [65] M. G. SWANSON, D. B. VIGNERON, T. K. TRAN, N. SAILASUTA, R. E. HURD, AND J. KURHANOWICZ. **Single-voxel oversampled J-resolved spectroscopy of in vivo human prostate tissue.** *Magn Reson Med*, **45**(6):973–980, Jun 2001. 6

REFERENCES

- [66] B. TURKBAY AND P. L. CHOYKE. **Multiparametric MRI and prostate cancer diagnosis and risk stratification.** *Curr Opin Urol*, **22**(4):310–315, Jul 2012. 7
- [67] L. WANG, Y. MAZAHARI, J. ZHANG, N. M. ISHILL, K. KUROIWA, AND H. HRICAK. **Assessment of biologic aggressiveness of prostate cancer: correlation of MR signal intensity with Gleason grade after radical prostatectomy.** *Radiology*, **246**(1):168–176, Jan 2008. 8, 9
- [68] O. AKIN, E. SALA, C. S. MOSKOWITZ, K. KUROIWA, N. M. ISHILL, D. PUCAR, P. T. SCARDINO, AND H. HRICAK. **Transition zone prostate cancers: features, detection, localization, and staging at endorectal MR imaging.** *Radiology*, **239**(3):784–792, Jun 2006. 8, 9
- [69] G. P. LINEY, M. LOWRY, L. W. TURNBULL, D. J. MANTON, A. J. KNOWLES, S. J. BLACKBAND, AND A. HORSMAN. **Proton MR T2 maps correlate with the citrate concentration in the prostate.** *NMR Biomed*, **9**(2):59–64, Apr 1996. 8, 9, 11
- [70] P. GIBBS, D. J. TOZER, G. P. LINEY, AND L. W. TURNBULL. **Comparison of quantitative T2 mapping and diffusion-weighted imaging in the normal and pathologic prostate.** *Magn Reson Med*, **46**(6):1054–1058, Dec 2001. 8, 11
- [71] W. LIU, B. TURKBAY, J. SENEGAS, S. REMMELE, S. XU, J. KRUECKER, M. BERNARDO, B. J. WOOD, P. A. PINTO, AND P. L. CHOYKE. **Accelerated T2 mapping for characterization of prostate cancer.** *Magn Reson Med*, **65**(5):1400–1406, May 2011. 8, 9
- [72] G. P. LINEY, L. W. TURNBULL, M. LOWRY, L. S. TURNBULL, A. J. KNOWLES, AND A. HORSMAN. **In vivo quantification of citrate concentration and water T2 relaxation time of the pathologic prostate gland using 1H MRS and MRI.** *Magn Reson Imaging*, **15**(10):1177–1186, 1997. 8, 9
- [73] S. VERMA, B. TURKBAY, N. MURADYAN, A. RAJESH, F. CORNUD, M. A. HAIDER, P. L. CHOYKE, AND M. HARISINGHANI. **Overview of dynamic contrast-enhanced MRI in prostate cancer diagnosis and management.** *AJR Am J Roentgenol*, **198**(6):1277–1288, Jun 2012. 8, 12, 13
- [74] P.S. TOFTS. **T1-weighted DCE imaging concepts: modelling, acquisition and analysis.** In *Magneton Flash*. Siemens, 2010. 8, 13
- [75] T. A. HUISMAN. **Diffusion-weighted imaging: basic concepts and application in cerebral stroke and head trauma.** *Eur Radiol*, **13**(10):2283–2297, Oct 2003. 8, 14, 15
- [76] T. HAMBROCK, D. M. SOMFORD, H. J. HUISMAN, I. M. VAN OORT, J. A. WITJES, C. A. HULSBERGEN-VAN DE KAA, T. SCHEENEN, AND J. O. BARENTSZ. **Relationship between apparent diffusion coefficients at 3.0-T MR imaging and Gleason grade in peripheral zone prostate cancer.** *Radiology*, **259**(2):453–461, May 2011. 8, 16
- [77] Y. ITOU, K. NAKANISHI, Y. NARUMI, Y. NISHIZAWA, AND H. TSUKUMA. **Clinical utility of apparent diffusion coefficient (ADC) values in patients with prostate cancer: can ADC values contribute to assess the aggressiveness of prostate cancer?** *J Magn Reson Imaging*, **33**(1):167–172, Jan 2011. 8, 16
- [78] Y. PENG, Y. JIANG, C. YANG, J.B. BROWN, T. ANTIC, I. SETHI, C. SCHMID-TANNWALD, M.L. GIGER, S.E. EGGNER, AND A. OTO. **Quantitative analysis of multiparametric prostate MR images: differentiation between prostate cancer and normal tissue and correlation with Gleason score—a computer-aided diagnosis development study.** *Radiology*, **267**(1):787–796, June 2013. 8, 16, 23, 47
- [79] S. VERMA, A. RAJESH, J. J. FUTTERER, B. TURKBAY, T. W. SCHEENEN, Y. PANG, P. L. CHOYKE, AND J. KURHANOWICZ. **Prostate MRI and 3D MR spectroscopy: how we do it.** *AJR Am J Roentgenol*, **194**(6):1414–1426, Jun 2010. 8
- [80] H. M. AWWAD, J. GEISEL, AND R. OBEID. **The role of choline in prostate cancer.** *Clin. Biochem.*, **45**(18):1548–1553, Dec 2012. 8, 17, 18
- [81] L. C. COSTELLO AND R. B. FRANKLIN. **The clinical relevance of the metabolism of prostate cancer; zinc and tumor suppression: connecting the dots.** *Mol. Cancer*, **5**:17, 2006. 8, 17
- [82] M. VAN DER GRAAF, R. G. SCHIPPER, G. O. OOSTERHOF, J. A. SCHALKEN, A. A. VERHOFSTAD, AND A. HEERSCHAP. **Proton MR spectroscopy of prostatic tissue focused on the detection of spermine, a possible biomarker of malignant behavior in prostate cancer.** *MAGMA*, **10**(3):153–159, Jul 2000. 8, 18
- [83] G. F. GISKEDEGARD, H. BERTILSSON, K. M. SELNAES, A. J. WRIGHT, T. F. BATHEN, T. VISET, J. HALGUNSET, A. ANGELSEN, I. S. GRIBBESTAD, AND M. B. TESSEM. **Spermine and citrate as metabolic biomarkers for assessing prostate cancer aggressiveness.** *PLoS ONE*, **8**(4):e62375, 2013. 8, 17, 18, 19
- [84] A. P. KIRKHAM, M. EMBERTON, AND C. ALLEN. **How good is MRI at detecting and characterising cancer within the prostate?** *Eur. Urol.*, **50**(6):1163–1174, Dec 2006. 9, 16
- [85] L. E. QUINT, J. S. VAN ERP, P. H. BLAND, S. H. MANDELL, E. A. DEL BUONO, H. B. GROSSMAN, G. M. GLAZER, AND P. W. GIKAS. **Carcinoma of the prostate: MR images obtained with body coils do not accurately reflect tumor volume.** *AJR Am J Roentgenol*, **156**(3):511–516, Mar 1991. 9
- [86] M. CRUZ, K. TSUDA, Y. NARUMI, Y. KUROIWA, T. NOSE, Y. KAJIMA, A. OKUYAMA, S. TAKAHASHI, K. AOZASA, J. O. BARENTSZ, AND H. NAKAMURA. **Characterization of low-intensity lesions in the peripheral zone of prostate on pre-biopsy endorectal coil MR imaging.** *Eur Radiol*, **12**(2):357–365, Feb 2002. 9
- [87] G. P. LINEY, A. J. KNOWLES, D. J. MANTON, L. W. TURNBULL, S. J. BLACKBAND, AND A. HORSMAN. **Comparison of conventional single echo and multi-echo sequences with a fast spin-echo sequence for quantitative T2 mapping: application to the prostate.** *J Magn Reson Imaging*, **6**(4):603–607, 1996. 11
- [88] INGRID S. GRIBBESTAD, KJELLI. GJESDAL, GUNNAR NILSEN, STEINAR LUNDGREN, MARI H. B. HJELSTUEN, AND ALAN JACKSON. **An introduction to dynamic contrast-enhanced MRI in oncology.** In ALAN JACKSON, DAVID L. BUCKLEY, AND GEOFFREY J. M. PARKER, editors, *Dynamic*

- Contrast-Enhanced Magnetic Resonance Imaging in Oncology*, Medical Radiology, pages 1–22. Springer Berlin Heidelberg, 2005. 12
- [89] A. R. PADHANI. **Dynamic contrast-enhanced MRI in clinical oncology: current status and future directions.** *J Magn Reson Imaging*, **16**(4):407–422, Oct 2002. 12
- [90] D. L. BUCKLEY, C. ROBERTS, G. J. PARKER, J. P. LOGUE, AND C. E. HUTCHINSON. **Prostate cancer: evaluation of vascular characteristics with dynamic contrast-enhanced T1-weighted MR imaging—initial experience.** *Radiology*, **233**(3):709–715, Dec 2004. 12
- [91] C. G. VAN NIEKERK, J. A. VAN DER LAAK, M. E. BORGER, H. J. HUISMAN, J. A. WITJES, J. O. BARENTSZ, AND C. A. HULSBERGEN-VAN DE KAA. **Computerized whole slide quantification shows increased microvascular density in pT2 prostate cancer as compared to normal prostate tissue.** *Prostate*, **69**(1):62–69, Jan 2009. 12
- [92] C. G. VAN NIEKERK, J. A. WITJES, J. O. BARENTSZ, J. A. VAN DER LAAK, AND C. A. HULSBERGEN-VAN DE KAA. **Microvascularity in transition zone prostate tumors resembles normal prostatic tissue.** *Prostate*, **73**(5):467–475, Apr 2013. 12, 13
- [93] P. CARMELIET AND R. K. JAIN. **Angiogenesis in cancer and other diseases.** *Nature*, **407**(6801):249–257, Sep 2000. 12
- [94] S.S. KETY. **The theory and applications of the exchange of inert gas at the lungs and tissues.** *Pharmacol. Rev.*, **3**(1):1–41, Mar 1951. 13
- [95] P. S. TOFTS. **Modeling tracer kinetics in dynamic Gd-DTPA MR imaging.** *J Magn Reson Imaging*, **7**(1):91–101, 1997. 13, 50
- [96] H. B. LARSSON, T. FRITZ-HANSEN, E. ROSTRUP, L. SONDERGAARD, P. RING, AND O. HENRIKSEN. **Myocardial perfusion modeling using MRI.** *Magn Reson Med*, **35**(5):716–726, May 1996. 13
- [97] K. S. ST LAWRENCE AND T. Y. LEE. **An adiabatic approximation to the tissue homogeneity model for water exchange in the brain: I. Theoretical derivation.** *J. Cereb. Blood Flow Metab.*, **18**(12):1365–1377, Dec 1998. 13
- [98] A. B. ROSENKRANTZ, A. SABACH, J. S. BABB, B. W. MATZA, S. S. TANEJA, AND F. M. DENG. **Prostate cancer: comparison of dynamic contrast-enhanced MRI techniques for localization of peripheral zone tumor.** *AJR Am J Roentgenol*, **201**(3):W471–478, Sep 2013. 13
- [99] G. J. JAGER, E. T. RUIJTER, C. A. VAN DE KAA, J. J. DE LA ROSETTE, G. O. OOSTERHOF, J. R. THORNBURY, S. H. RULIS, AND J. O. BARENTSZ. **Dynamic TurboFLASH subtraction technique for contrast-enhanced MR imaging of the prostate: correlation with histopathologic results.** *Radiology*, **203**(3):645–652, Jun 1997. 13
- [100] J. K. KIM, S. S. HONG, Y. J. CHOI, S. H. PARK, H. AHN, C. S. KIM, AND K. S. CHO. **Wash-in rate on the basis of dynamic contrast-enhanced MRI: usefulness for prostate cancer detection and localization.** *J Magn Reson Imaging*, **22**(5):639–646, Nov 2005. 13
- [101] H. P. SCHLEMMER, J. MERKLE, R. GROBHOLZ, T. JAEGER, M. S. MICHEL, A. WERNER, J. RABE, AND G. VAN KAICK. **Can pre-operative contrast-enhanced dynamic MR imaging for prostate cancer predict microvessel density in prostatectomy specimens?** *Eur Radiol*, **14**(2):309–317, Feb 2004. 13
- [102] B. ZELHOF, M. LOWRY, G. RODRIGUES, S. KRAUS, AND L. TURNBULL. **Description of magnetic resonance imaging-derived enhancement variables in pathologically confirmed prostate cancer and normal peripheral zone regions.** *BJU Int.*, **104**(5):621–627, Sep 2009. 13
- [103] D. LE BIHAN, E. BRETON, D. LALLEMAND, M. L. AUBIN, J. VIGNAUD, AND M. LAVAL-JEANTET. **Separation of diffusion and perfusion in intravoxel incoherent motion MR imaging.** *Radiology*, **168**(2):497–505, Aug 1988. 14
- [104] D. M. KOH AND D. J. COLLINS. **Diffusion-weighted MRI in the body: applications and challenges in oncology.** *AJR Am J Roentgenol*, **188**(6):1622–1635, Jun 2007. 14
- [105] D. M. SOMFORD, J. J. FUTTERER, T. HAMBROCK, AND J. O. BARENTSZ. **Diffusion and perfusion MR imaging of the prostate.** *Magn Reson Imaging Clin N Am*, **16**(4):685–695, Nov 2008. 14
- [106] D. LE BIHAN, E. BRETON, D. LALLEMAND, P. GRENIER, E. CABBANIS, AND M. LAVAL-JEANTET. **MR imaging of intravoxel incoherent motions: application to diffusion and perfusion in neurologic disorders.** *Radiology*, **161**(2):401–407, Nov 1986. 15, 16
- [107] R. SHIMOFUSA, H. FUJIMOTO, H. AKAMATA, K. MOTOORI, S. YAMAMOTO, T. UEDA, AND H. ITO. **Diffusion-weighted imaging of prostate cancer.** *J Comput Assist Tomogr*, **29**(2):149–153, 2005. 15
- [108] A. R. PADHANI. **Integrating multiparametric prostate MRI into clinical practice.** *Cancer Imaging*, **11 Spec No A**:27–37, 2011. 15
- [109] K. W. DOO, D. J. SUNG, B. J. PARK, M. J. KIM, S. B. CHO, Y. W. OH, Y. H. KO, AND K. S. YANG. **Detectability of low and intermediate or high risk prostate cancer with combined T2-weighted and diffusion-weighted MRI.** *Eur Radiol*, **22**(8):1812–1819, Aug 2012. 16
- [110] E.M. HAACKE, R.W. BROWN, M.R. THOMPSON, AND R. VENKATESAN. *Magnetic resonance imaging: Physical principles and sequence design.* Wiley, 1999. 18
- [111] G. LEMAÎTRE. *Absolute quantification at 3 T.* Master’s thesis, Université de Bourgogne, Heriot-Watt University, Universitat de Girona, 2011. 18, 19
- [112] J. SCHEIDLER, H. HRICAK, D. B. VIGNERON, K. K. YU, D. L. SOKOLOV, L. R. HUANG, C. J. ZALOUDEK, S. J. NELSON, P. R. CARROLL, AND J. KURHANOWICZ. **Prostate cancer: localization with three-dimensional proton MR spectroscopic imaging—clinicopathologic study.** *Radiology*, **213**(2):473–480, Nov 1999. 19

REFERENCES

- [113] Y. KAJI, J. KURHANOWICZ, H. HRICAK, D. L. SOKOLOV, L. R. HUANG, S. J. NELSON, AND D. B. VIGNERON. **Localizing prostate cancer in the presence of postbiopsy changes on MR images: role of proton MR spectroscopic imaging.** *Radiology*, **206**(3):785–790, Mar 1998. 19
- [114] JOAN C VILANOVA, JOSEP COMET, CARLES BARCELÓ-VIDAL, JOAQUIM BARCELÓ, EUGENI LÓPEZ-BONET, ALBERT MAROTO, MONTSE ARZO, ÀNGEL MORENO, AND JOAN AREAL. **Peripheral zone prostate cancer in patients with elevated PSA levels and low free-to-total PSA ratio: detection with MR imaging and MR spectroscopy.** *Radiology*, **253**(1):135–143, 2009. 19
- [115] P.M. WALKER, G. CREHANGE, S. PARFAIT, A. COCHET, P. MAIGNON, L. CORMIER, AND F. BRUNOTTE. **Absolute quantification in 1H MRSI of the prostate at 3T.** In *ISMRM Annual Meeting 2010*, 2010. 19
- [116] D. AMPELIOTIS, A. ANONAKOUDI, K. BERBERIDIS, AND E. Z. PSARAKIS. **Computer aided detection of prostate cancer using fused information from dynamic contrast enhanced and morphological magnetic resonance images.** In *IEEE International Conference on Signal Processing and Communications*, pages 888–891, 2007. 23, 25, 35, 42, 44, 47, 48
- [117] D. AMPELIOTIS, A. ANONAKOUDI, K. BERBERIDIS, E. Z. PSARAKIS, AND A. KOUNOUDIS. **A computer-aided system for the detection of prostate cancer based on magnetic resonance image analysis.** In *International Symposium on Communications, Control and Signal Processing*, 2008. 23, 25, 35, 42, 44, 47, 48
- [118] TATJANA ANTIC, YAHUI PENG, YULEI JIANG, MARYELLEN L. GIGER, SCOTT EGGNER, AND AYTEKIN OTO. **A study of T2-weighted MR image texture features and diffusion-weighted MR image features for computer-aided diagnosis of prostate cancer.** In *Proc. SPIE 8670, Medical Imaging 2013: Computer-Aided Diagnosis*, pages 86701H–86701H–6, 2013. 23, 45, 47
- [119] Y. ARTAN, D.L. LANGER, M.A. HAIDER, T. H. VAN DER KWAST, A.J. EVANS, M.N. WERNICK, AND I.S. YETIK. **Prostate cancer segmentation with multispectral MRI using cost-sensitive Conditional Random Fields.** In *Biomedical Imaging: From Nano to Macro, 2009. ISBI '09. IEEE International Symposium on*, pages 278–281, 2009. 23, 29, 35, 36, 43, 44, 50
- [120] Y. ARTAN, M. A. HAIDER, D. L. LANGER, T. H. VAN DER KWAST, A. J. EVANS, Y. YANG, M. N. WERNICK, J. TRACHTENBERG, AND I. S. YETIK. **Prostate cancer localization with multispectral MRI using cost-sensitive support vector machines and conditional random fields.** *IEEE Trans Image Process*, **19**(9):2444–2455, Sep 2010. 23, 29, 35, 36, 43, 44, 50
- [121] I. CHAN, W. WELLS, R. V. MULKERN, S. HAKER, J. ZHANG, K. H. ZOU, S. E. MAIER, AND C. M. TEMPANY. **Detection of prostate cancer by integration of line-scan diffusion, T2-mapping and T2-weighted magnetic resonance imaging; a multichannel statistical classifier.** *Med Phys*, **30**(9):2390–2398, Sep 2003. 23, 44, 47
- [122] V. GIANNINI, A. VIGNATI, S. MAZZETTI, M. DE LUCA, C. BRACCO, M. STASI, F. RUSSO, E. ARMANDO, AND D. REGGE. **A prostate CAD system based on multiparametric analysis of DCE T1-w, and DW automatically registered images.** In *Proc. SPIE 8670, Medical Imaging 2013: Computer-Aided Diagnosis*, pages 86703E–86703E–6, 2013. 23, 42, 43, 50, 51
- [123] B. M. KELM, B. H. MENZE, C. M. ZECHMANN, K. T. BAUDENDISTEL, AND F. A. HAMPRECHT. **Automated estimation of tumor probability in prostate magnetic resonance spectroscopic imaging: pattern recognition vs quantification.** *Magn Reson Med*, **57**(1):150–159, Jan 2007. 23, 32, 35, 43, 51
- [124] D. L. LANGER, T. H. VAN DER KWAST, A. J. EVANS, J. TRACHTENBERG, B. C. WILSON, AND M. A. HAIDER. **Prostate cancer detection with multi-parametric MRI: logistic regression analysis of quantitative T2, diffusion-weighted imaging, and dynamic contrast-enhanced MRI.** *J Magn Reson Imaging*, **30**(2):327–334, Aug 2009. 23, 44, 50
- [125] G. J. S. LITJENS, P. C. VOS, J. O. BARENTSZ, N. KARSEMELJER, AND H. J. HUISMAN. **Automatic computer aided detection of abnormalities in multi-parametric prostate MRI.** In *Proc. SPIE 7963, Medical Imaging 2011: Computer-Aided Diagnosis*, pages 79630T–79630T–7, 2011. 23, 35, 37, 43, 44, 47
- [126] G. J. S. LITJENS, J. O. BARENTSZ, N. KARSEMELJER, AND H. J. HUISMAN. **Automated computer-aided detection of prostate cancer in MR images: from a whole-organ to a zone-based approach.** In *Proc. SPIE 8315, Medical Imaging 2012: Computer-Aided Diagnosis*, pages 83150G–83150G–6, 2012. 23, 35, 36, 43, 44, 47
- [127] G. LITJENS, O. DEBATS, J. BARENTSZ, N. KARSEMELJER, AND H. HUISMAN. **Computer-aided detection of prostate cancer in MRI.** *Medical Imaging, IEEE Transactions on*, **33**(5):1083–1092, May 2014. 23, 35, 36, 43
- [128] X. LIU, D. L. LANGER, M. A. HAIDER, Y. YANG, M. N. WERNICK, AND I. S. YETIK. **Prostate cancer segmentation with simultaneous estimation of Markov random field parameters and class.** *IEEE Trans Med Imaging*, **28**(6):906–915, Jun 2009. 23, 43, 44, 50
- [129] P. LIU, S. WANG, B. TURKBAY, P. AND CHOYKE P. GRANT, K. AND PINTO, B. J. WOOD, AND R. M. SUMMERS. **A prostate cancer computer-aided diagnosis system using multimodal magnetic resonance imaging and targeted biopsy labels.** In *Proc. SPIE 8670, Medical Imaging 2013: Computer-Aided Diagnosis*, pages 86701G–86701G–6, 2013. 23, 29, 47, 48
- [130] R. LOPES, A. AYACHE, N. MAKNI, P. PUECH, A. VILLERS, S. MORDON, AND N. BETROUNI. **Prostate cancer characterization on MR images using fractal features.** *Med Phys*, **38**(1):83–95, Jan 2011. 23, 25, 35, 43, 47, 48
- [131] D. LV, X. GUO, X. WANG, J. ZHANG, AND J. FANG. **Computerized characterization of prostate cancer by fractal analysis in MR images.** *J Magn Reson Imaging*, **30**(1):161–168, Jul 2009. 23, 28, 29, 35, 48
- [132] LUKASZ MATULEWICZ, JACOBUS F.A. JANSSEN, LOUISA BOKACHEVA, HEBERT ALBERTO VARGAS, OGUZ AKIN, SAMSON W. FINE, AMITA SHUKLA-DAVE, JAMES A. EASTHAM, HEDVIG HRICAK, JASON A. KOUTCHER, AND KRISTEN L. ZAKIAN. **Anatomic segmentation improves prostate cancer detection with artificial neural networks analysis of 1H magnetic resonance spectroscopic imaging.** *Journal of Magnetic Resonance Imaging*, pages n/a–n/a, 2013. 23, 35, 36, 43, 47, 51

- [133] S. MAZZETTI, M. DE LUCA, C. BRACCO, A. VIGNATI, V. GIANNINI, M. STASI, F. RUSSO, E. ARMANDO, S. AGLIOZZO, AND D. REGGE. **A CAD system based on multi-parametric analysis for cancer prostate detection on DCE-MRI.** In *Proc. SPIE 7963, Medical Imaging 2011: Computer-Aided Diagnosis*, pages 79633Q–79633Q–7, 2011. 23, 43, 50, 51
- [134] S. OZER, M.A. HAIDER, D. L. LANGER, T. H. VAN DER KWAST, A.J. EVANS, M.N. WERNICK, J. TRACHTENBERG, AND I.S. YETIK. **Prostate cancer localization with multi-spectral MRI based on Relevance Vector Machines.** In *Biomedical Imaging: From Nano to Macro, 2009. ISBI '09. IEEE International Symposium on*, pages 73–76, 2009. 23, 25, 29, 35, 36, 43, 50
- [135] S. OZER, D. L. LANGER, X. LIU, M. A. HAIDER, T. H. VAN DER KWAST, A. J. EVANS, Y. YANG, M. N. WERNICK, AND I. S. YETIK. **Supervised and unsupervised methods for prostate cancer segmentation with multispectral MRI.** *Med Phys*, **37**(4):1873–1883, Apr 2010. 23, 25, 29, 35, 36, 43, 50
- [136] S. PARFAIT, P.M. WALKER, G. CRHANGE, X. TIZON, AND J. MITRAN. **Classification of prostate magnetic resonance spectra using Support Vector Machine.** *Biomedical Signal Processing and Control*, **7**(5):499 – 508, 2012. 23, 30, 33, 34, 35, 43, 51
- [137] P. PUECH, N. BETROUNI, N. MAKNI, A. S. DEWALLE, A. VILLERS, AND L. LEMAITRE. **Computer-assisted diagnosis of prostate cancer using DCE-MRI data: design, implementation and preliminary results.** *Int J Comput Assist Radiol Surg*, **4**(1):1–10, Jan 2009. 23, 35, 36
- [138] Y. S. SUNG, H. J. KWON, B. W. PARK, G. CHO, C. K. LEE, K. S. CHO, AND J. K. KIM. **Prostate cancer detection on dynamic contrast-enhanced MRI: computer-aided diagnosis versus single perfusion parameter maps.** *AJR Am J Roentgenol*, **197**(5):1122–1129, Nov 2011. 23, 43, 50
- [139] P. TIWARI, A. MADABHUSHI, AND M. ROSEN. **A hierarchical unsupervised spectral clustering scheme for detection of prostate cancer from magnetic resonance spectroscopy (MRS).** *Med Image Comput Comput Assist Interv*, **10**(Pt 2):278–286, 2007. 23, 43, 51
- [140] P. TIWARI, M. ROSEN, AND A. MADABHUSHI. **Consensus-locally linear embedding (C-LLE): application to prostate cancer detection on magnetic resonance spectroscopy.** *Med Image Comput Comput Assist Interv*, **11**(Pt 2):330–338, 2008. 23, 43
- [141] P. TIWARI, M. ROSEN, AND A. MADABHUSHI. **A hierarchical spectral clustering and nonlinear dimensionality reduction scheme for detection of prostate cancer from magnetic resonance spectroscopy (MRS).** *Med Phys*, **36**(9):3927–3939, Sep 2009. 23, 35, 37, 43, 51
- [142] P. TIWARI, M. ROSEN, G. REED, J. KURHANEWICZ, AND A. MADABHUSHI. **Spectral embedding based probabilistic boosting tree (ScEPTre): classifying high dimensional heterogeneous biomedical data.** *Med Image Comput Comput Assist Interv*, **12**(Pt 2):844–851, 2009. 23, 43, 45, 47, 51
- [143] P. TIWARI, J. KURHANEWICZ, M. ROSEN, AND A. MADABHUSHI. **Semi supervised multi kernel (SeSMiK) graph embedding: identifying aggressive prostate cancer via magnetic resonance imaging and spectroscopy.** *Med Image Comput Comput Assist Interv*, **13**(Pt 3):666–673, 2010. 23, 43, 45, 47, 51
- [144] P. TIWARI, S. VISWANATH, J. KURHANEWICZ, A. SRIDHAR, AND A. MADABHUSHI. **Multimodal wavelet embedding representation for data combination (MaW-ERiC): integrating magnetic resonance imaging and spectroscopy for prostate cancer detection.** *NMR Biomed*, **25**(4):607–619, Apr 2012. 23, 33, 34, 35, 43, 45, 48, 51
- [145] P. TIWARI, J. KURHANEWICZ, AND A. MADABHUSHI. **Multi-kernel graph embedding for detection, Gleason grading of prostate cancer via MRI/MRS.** *Med Image Anal*, **17**(2):219–235, Feb 2013. 23, 43, 45, 47, 51
- [146] S. VISWANATH, P. TIWARI, M. ROSEN, AND A. MADABHUSHI. **A meta-classifier for detecting prostate cancer by quantitative integration of In Vivo magnetic resonance spectroscopy and magnetic resonance imaging.** In *Medical Imaging 2008: Computer-Aided Diagnosis*, **6915**. SPIE, 2008. 23, 43, 45, 47, 48
- [147] S. VISWANATH, B. N. BLOCH, E. GENEGA, N. ROFSKY, R. LENKINSKI, J. CHAPPELOW, R. TOTH, AND A. MADABHUSHI. **A comprehensive segmentation, registration, and cancer detection scheme on 3 Tesla in vivo prostate DCE-MRI.** *Med Image Comput Comput Assist Interv*, **11**(Pt 1):662–669, 2008. 23, 35, 36, 42, 43, 44, 45, 47, 48, 51
- [148] S. VISWANATH, B. N. BLOCH, M. ROSEN, J. CHAPPELOW, R. TOTH, N. ROFSKY, R. LENKINSKI, E. GENEGA, A. KALYANPUR, AND A. MADABHUSHI. **Integrating structural and functional imaging for computer assisted detection of prostate cancer on multi-protocol in vivo 3 Tesla MRI.** In *Society of Photo-Optical Instrumentation Engineers (SPIE) Conference Series*, **7260** of *Society of Photo-Optical Instrumentation Engineers (SPIE) Conference Series*, February 2009. 23, 26, 29, 35, 36, 42, 43
- [149] S. VISWANATH, B. N. BLOCH, J. CHAPPELOW, P. PATEL, N. ROFSKY, R. LENKINSKI, E. GENEGA, AND A. MADABHUSHI. **Enhanced multi-protocol analysis via intelligent supervised embedding (EMPrAvISE): detecting prostate cancer on multi-parametric MRI.** In *Proc. SPIE 7963, Medical Imaging 2011: Computer-Aided Diagnosis*, 2011. 23, 29, 35, 42, 43, 44, 45, 47
- [150] S. E. VISWANATH, N. B. BLOCH, J. C. CHAPPELOW, R. TOTH, N. M. ROFSKY, E. M. GENEGA, R. E. LENKINSKI, AND A. MADABHUSHI. **Central gland and peripheral zone prostate tumors have significantly different quantitative imaging signatures on 3 Tesla endorectal, in vivo T2-weighted MR imagery.** *J Magn Reson Imaging*, **36**(1):213–224, Jul 2012. 23, 27, 29, 35, 37, 43, 45, 47
- [151] P. C. VOS, T. HAMBROCK, J. O. BARENSTZ, AND H. J. HUISMAN. **Combining T2-weighted with dynamic MR images for computerized classification of prostate lesions.** In *Medical Imaging 2008: Computer-Aided Diagnosis*, **6915**. SPIE, 2008. 23, 35, 36, 42, 47

REFERENCES

- [152] P. C. VOS, T. HAMBROCK, C. A. HULSBERGEN-VAN DE KAA, J. J. FUTTERER, J. O. BARENTSZ, AND H. J. HUISMAN. **Computerized analysis of prostate lesions in the peripheral zone using dynamic contrast enhanced MRI.** *Med Phys*, **35**(3):888–899, Mar 2008. 23, 35, 36, 47
- [153] P. C. VOS, T. HAMBROCK, J. O. BARENTSZ, AND H. J. HUISMAN. **Computer-assisted analysis of peripheral zone prostate lesions using T2-weighted and dynamic contrast enhanced T1-weighted MRI.** *Phys Med Biol*, **55**(6):1719–1734, Mar 2010. 23, 35, 42, 44, 47
- [154] P. C. VOS, J. O. BARENTSZ, N. KARSEMELIER, AND H. J. HUISMAN. **Automatic computer-aided detection of prostate cancer based on multiparametric magnetic resonance image analysis.** *Phys Med Biol*, **57**(6):1527–1542, Mar 2012. 23, 35, 37, 43, 47
- [155] R.D. NOWAK. **Wavelet-based Rician noise removal for magnetic resonance imaging.** *Image Processing, IEEE Transactions on*, **8**(10):1408–1419, 1999. 24, 25
- [156] J. V. MANJON, J. CARBONELL-CABALLERO, J. J. LULL, G. GARCIA-MARTI, L. MARTI-BONMATI, AND M. ROBLES. **MRI denoising using non-local means.** *Med Image Anal*, **12**(4):514–523, Aug 2008. 25
- [157] A. BUADES, B. COLL, AND J.M. MOREL. **A review of image denoising algorithms, with a new one.** *Simul*, **4**:490–530, 2005. 25
- [158] J. MOHAN, V. KRISHNAVENI, AND Y. GUO. **A survey on the magnetic resonance image denoising methods.** *Biomedical Signal Processing and Control*, **9**(0):56 – 69, 2014. 25
- [159] D. L. DONOHO AND J. M. JOHNSTONE. **Ideal spatial adaptation by wavelet shrinkage.** *Biometrika*, **81**(3):425–455, 1994. 25
- [160] ALEKSANDRA PIZURICA. *Image denoising using wavelets and spatial context modeling.* PhD thesis, Universiteit Gent, 2002. 25
- [161] S. MALLAT. *A wavelet tour of signal processing, Third Edition: The sparse way.* Academic Press, 3rd edition, 2008. 25
- [162] A. PIZURICA, W. PHILIPS, I. LEMAHIEU, AND M. ACHEROY. **A versatile wavelet domain noise filtration technique for medical imaging.** *IEEE Trans Med Imaging*, **22**(3):323–331, Mar 2003. 25
- [163] M. STYNER, C. BRECHBUHLER, G. SZCKELY, AND G. GERIG. **Parametric estimate of intensity inhomogeneities applied to MRI.** *Medical Imaging, IEEE Transactions on*, **19**(3):153–165, 2000. 26
- [164] M. JUNGKE, W. VON SEELEN, G. BIELKE, S. MEINDL, M. GRIGAT, AND P. PFANNENSTIEL. **A system for the diagnostic use of tissue characterizing parameters in NMR-tomography.** In *Proc. of Information Processing in Medical Imaging*, **87**, pages 471–481, 1987. 26
- [165] U. VOVK, F. PERNUS, AND B. LIKAR. **A review of methods for correction of intensity inhomogeneity in MRI.** *Medical Imaging, IEEE Transactions on*, **26**(3):405–421, 2007. 26
- [166] S. Z. LI. **Robustizing robust M-estimation using deterministic annealing.** *Pattern Recognition*, **29**:159–166, 1996. 27
- [167] M. STYNER AND G. GERIG. **Evaluation of 2D/3D bias correction with 1+1ES-optimization.** Technical report, ETH Zürich, 1997. 27
- [168] J. G. SLED, A. P. ZIJDENBOS, AND A. C. EVANS. **A nonparametric method for automatic correction of intensity nonuniformity in MRI data.** *IEEE Trans Med Imaging*, **17**(1):87–97, Feb 1998. 27
- [169] A. MADABHUSHI, J.K. UDUPA, AND A. SOUZA. **Generalized scale: Theory, algorithms, and application to image inhomogeneity correction.** *Computer Vision and Image Understanding*, **101**(2):100 – 121, 2006. 28
- [170] L. G. SHAPIRO AND G. C. STOCKMAN. *Computer vision.* Prentice Hall, Upper Saddle River, NJ, 2001. 28
- [171] L. G. NYUL AND J. K. UDUPA. **On standardizing the MR image intensity scale.** *Magn Reson Med*, **42**(6):1072–1081, Dec 1999. 28
- [172] A. MADABHUSHI AND J. K. UDUPA. **New methods of MR image intensity standardization via generalized scale.** *Med Phys*, **33**(9):3426–3434, Sep 2006. 29
- [173] M. WIART, L. CUIEL, A. GELET, D. LYONNET, J. Y. CHAPELON, AND O. ROUVIERE. **Influence of perfusion on high-intensity focused ultrasound prostate ablation: a first-pass MRI study.** *Magn Reson Med*, **58**(1):119–127, Jul 2007. 30
- [174] LI CHEN, ZHIQIANG WENG, LAIYOONG GOH, AND MARC GARLAND. **An efficient algorithm for automatic phase correction of {NMR} spectra based on entropy minimization.** *Journal of Magnetic Resonance*, **158**(12):164 – 168, 2002. 30, 32, 33
- [175] M.I. OSORIO-GARCIA, A.R. CROITOR SAVA, D. M. SIMA, F.U. NIELSEN, U. HIMMELREICH, AND S. VAN HUFFEL. *Magnetic Resonance Spectroscopy*, chapter Quantification improvements of 1H MRS Signals, pages 1–27. InTech, March 2012. 30, 32, 33
- [176] H. ZHU, R. OUWERKERK, AND P. B. BARKER. **Dual-band water and lipid suppression for MR spectroscopic imaging at 3 Tesla.** *Magn Reson Med*, **63**(6):1486–1492, Jun 2010. 32
- [177] W.W.F. PLUNAPPEL, A. VAN DEN BOOGAART, R. DE BEER, AND D. VAN ORMONDT. **SVD-based quantification of magnetic resonance signals.** *Journal of Magnetic Resonance (1969)*, **97**(1):122 – 134, 1992. 32, 33
- [178] T. LAUDADIO, N. MASTRONARDI, L. VANHAMME, P. VAN HECKE, AND S. VAN HUFFEL. **Improved Lanczos algorithms for blackbox {MRS} data quantitation.** *Journal of Magnetic Resonance*, **157**(2):292 – 297, 2002. 33
- [179] C. A. LIEBER AND A. MAHADEVAN-JANSEN. **Automated method for subtraction of fluorescence from biological Raman spectra.** *Appl Spectrosc*, **57**(11):1363–1367, Nov 2003. 33
- [180] A. DEVOS, L. LUKAS, J. A. SUYKENS, L. VANHAMME, A. R. TATE, F. A. HOWE, C. MAJOS, A. MORENO-TORRES, M. VAN DER GRAAF, C. ARUS, AND S. VAN HUFFEL. **Classification of brain tumours using short echo time 1H MR spectra.** *J. Magn. Reson.*, **170**(1):164–175, Sep 2004. 33, 34

-
- [181] S. GHOSE, A. OLIVER, R. MARTI, X. LLADO, J. C. VILANOVA, J. FREIXENET, J. MITRA, D. SIDIBE, AND F. MERIAUDEAU. **A survey of prostate segmentation methodologies in ultrasound, magnetic resonance and computed tomography images.** *Comput Methods Programs Biomed*, **108**(1):262–287, Oct 2012. 34
- [182] G. LITJENS, O. DEBATS, W. VAN DE VEN, N. KARSSEMEIJER, AND H. HUISMAN. **A pattern recognition approach to zonal segmentation of the prostate on MRI.** *Med Image Comput Comput Assist Interv*, **15**(Pt 2):413–420, 2012. 36
- [183] S. K. WARFIELD, K. H. ZOU, AND W. M. WELLS. **Simultaneous truth and performance level estimation (STAPLE): an algorithm for the validation of image segmentation.** *IEEE Trans Med Imaging*, **23**(7):903–921, Jul 2004. 36
- [184] M. AMADASUN AND R. KING. **Textural features corresponding to textural properties.** *Systems, Man and Cybernetics, IEEE Transactions on*, **19**(5):1264–1274, 1989. 36
- [185] H. LI, M. L. GIGER, O. I. OLOPADE, A. MARGOLIS, L. LAN, AND M. R. CHINANDER. **Computerized texture analysis of mammographic parenchymal patterns of digitized mammograms.** *Acad Radiol*, **12**(7):863–873, Jul 2005. 36
- [186] T. OJALA, M. PIETIKÄINEN, AND D. HARWOOD. **A comparative study of texture measures with classification based on featured distributions.** *Pattern Recognition*, **29**(1):51–59, January 1996. 36, 48
- [187] F. L. BOOKSTEIN. **Principal warps: thin-plate splines and the decomposition of deformations.** *Pattern Analysis and Machine Intelligence, IEEE Transactions on*, **11**(6):567–585, 1989. 36
- [188] G. LITJENS, R. TOTH, W. VAN DE VEN, C. HOEKS, S. KERKSTRA, B. VAN GINNEKEN, G. VINCENT, G. GUILLARD, N. BIRBECK, J. ZHANG, R. STRAND, F. MALMBERG, Y. OU, C. DAVATZIKOS, M. KIRSCHNER, F. JUNG, J. YUAN, W. QIU, Q. GAO, P. E. EDWARDS, B. MAAN, F. VAN DER HEIDEN, S. GHOSE, J. MITRA, J. DOWLING, D. BARRATT, H. HUISMAN, AND A. MADABHUSHI. **Evaluation of prostate segmentation algorithms for MRI: the PROMISE12 challenge.** *Med Image Anal*, **18**(2):359–373, Feb 2014. 36
- [189] THOMAS ROBIN LANGERAK, UULKE A VAN DER HEIDE, ALEXIS NTJ KOTTE, MAX A VIERGEVER, MARCO VAN VULPEN, AND JOSIEN PW PLUIM. **Label fusion in atlas-based segmentation using a selective and iterative method for performance level estimation (SIMPLE).** *IEEE Transactions on Medical Imaging*, **29**(12):2000–2008, 2010. 36
- [190] R. TOTH, J. CHAPPELOW, M. ROSEN, S. PUNGAVKAR, A. KALYANPUR, AND A. MADABHUSHI. **Multi-attribute non-initializing texture reconstruction based active shape model (MANTRA).** *Med Image Comput Comput Assist Interv*, **11**(Pt 1):653–661, 2008. 36, 40
- [191] T. F. COOTES, C. J. TAYLOR, D. H. COOPER, AND J. GRAHAM. **Active shape models and their training and application.** *Comput. Vis. Image Underst.*, **61**(1):38–59, January 1995. 36, 37
- [192] K. PEARSON. **On lines and planes of closest fit to systems of points in space.** *Philosophical Magazine*, **2**(6):559–572, 1901. 37
- [193] R TOTH, S. DOYLE, S PUNGAVKAR, A KALYANPUR, AND A MADABHUSHI. **A boosted ensemble scheme for accurate landmark detection for active shape models.** In *SPIE Medical Imaging*, **7260**, Orlando, FL, 2009. 37, 40
- [194] H. HUISMAN, P.C. VOS, G. LITJENS, T. HAMBROCK, AND J. BARENTSZ. **Computer aided detection of prostate cancer using T2, DWI and DCE MRI: methods and clinical applications.** In *Proceedings of the 2010 international conference on Prostate cancer imaging: computer-aided diagnosis, prognosis, and intervention, MICCAI’10*, pages 4–14, Berlin, Heidelberg, 2010. Springer-Verlag. 37
- [195] J. SHI AND J. MALIK. **Normalized cuts and image segmentation.** *Pattern Analysis and Machine Intelligence, IEEE Transactions on*, **22**(8):888–905, 2000. 37
- [196] M. BELKIN AND P. NIYOGI. **Laplacian eigenmaps and spectral techniques for embedding and clustering.** In *Advances in Neural Information Processing Systems 14*, pages 585–591. MIT Press, 2001. 38
- [197] J. B. MAINTZ AND M. A. VIERGEVER. **A survey of medical image registration.** *Med Image Anal*, **2**(1):1–36, Mar 1998. 39
- [198] B. ZITOVÁ AND J. FLUSSER. **Image registration methods: a survey.** *Image and Vision Computing*, **21**(11):977 – 1000, 2003. 39
- [199] J. MITRA, R. MARTI, A. OLIVER, X. LLADO, J. C. VILANOVA, AND F. MERIAUDEAU. **A comparison of thin-plate splines with automatic correspondences and B-splines with uniform grids for multimodal prostate registration.** In *Society of Photo-Optical Instrumentation Engineers (SPIE) Conference Series*, **7964** of *Society of Photo-Optical Instrumentation Engineers (SPIE) Conference Series*, March 2011. 40
- [200] J. MITRA, Z. KATO, R. MARTI, A. OLIVER, X. LLADO, D. SIDIBE, S. GHOSE, J. C. VILANOVA, J. COMET, AND F. MERIAUDEAU. **A spline-based non-linear diffeomorphism for multimodal prostate registration.** *Med Image Anal*, **16**(6):1259–1279, Aug 2012. 40
- [201] J.P.W. PLUIM, J.B.A. MAINTZ, AND M.A. VIERGEVER. **Mutual-information-based registration of medical images: a survey.** *IEEE Transactions on Medical Imaging*, **22**(8):986–1004, 2003. 41
- [202] J. CHAPPELOW, B. N. BLOCH, N. ROFSKY, E. GENEGA, R. LENKINSKI, W. DEWOLF, AND A. MADABHUSHI. **Elastic registration of multimodal prostate MRI and histology via multiattribute combined mutual information.** *Med Phys*, **38**(4):2005–2018, Apr 2011. 41, 42
- [203] RICHARD H. BYRD, PEI HUANG LU, JORGE NOCEDAL, AND CIYOU ZHU. **A limited memory algorithm for bound constrained optimization.** *SIAM J. Sci. Comput.*, **16**(5):1190–1208, September 1995. 41
- [204] P. VIOLA AND W. M. WELLS, III. **Alignment by maximization of mutual information.** *Int. J. Comput. Vision*, **24**(2):137–154, September 1997. 41

REFERENCES

- [205] J. MITRA. *Multimodal image registration applied to magnetic resonance and ultrasound prostatic images*. PhD thesis, Universitat de Girona and Université de Bourgogne, 2012. 41
- [206] D. RUECKERT, L. I. SONODA, C. HAYES, D. L. HILL, M. O. LEACH, AND D. J. HAWKES. **Nonrigid registration using free-form deformations: application to breast MR images**. *IEEE Trans Med Imaging*, **18**(8):712–721, Aug 1999. 42
- [207] Q. LI, S. SONE, AND K. DOI. **Selective enhancement filters for nodules, vessels, and airway walls in two- and three-dimensional CT scans**. *Med Phys*, **30**(8):2040–2051, Aug 2003. 43
- [208] J.M.S. PREWITT. *Picture processing and psychohistories*, chapter Object enhancement and extraction. Academic Press, 1970. 45
- [209] I. SOBEL. **Camera models and machine perception**. Technical report, DTIC Document, 1970. 45
- [210] R.A. KIRSCH. **Computer determination of the constituent structure of biological images**. *Computers and Biomedical Research*, **4**(3):315 – 328, 1971. 45
- [211] D. GABOR. **Theory of communication. Part 1: The analysis of information**. *Electrical Engineers - Part III: Radio and Communication Engineering, Journal of the Institution of*, **93**(26):429–441, 1946. 45
- [212] J. G. DAUGMAN. **Uncertainty relation for resolution in space, spatial frequency, and orientation optimized by two-dimensional visual cortical filters**. *J Opt Soc Am A*, **2**(7):1160–1169, Jul 1985. 45
- [213] A. BENASSI, S. COHEN, AND J. ISTAS. **Identifying the multifractional function of a Gaussian process**. *Statistics & Probability Letters*, **39**(4):337 – 345, 1998. 47
- [214] N. AHMED, T. NATARAJAN, AND K.R. RAO. **Discrete cosine transform**. *Computers, IEEE Transactions on*, **C-23**(1):90–93, 1974. 47
- [215] N. DALAL AND B. TRIGGS. **Histograms of oriented gradients for human detection**. In *Computer Vision and Pattern Recognition, 2005. CVPR 2005. IEEE Computer Society Conference on*, **1**, pages 886–893 vol. 1, 2005. 47
- [216] S. BELONGIE, J. MALIK, AND J. PUZICHA. **Shape matching and object recognition using shape contexts**. *Pattern Analysis and Machine Intelligence, IEEE Transactions on*, **24**(4):509–522, 2002. 48
- [217] G. ZHAO, T. AHONEN, J. MATAS, AND M. PIETIKAINEN. **Rotation-Invariant Image and Video Description With Local Binary Pattern Features**. *Image Processing, IEEE Transactions on*, **21**(4):1465–1477, 2012. 48
- [218] P. CASTORINA, P. P. DELSANTO, AND C. GUIOT. **Classification scheme for phenomenological universalities in growth problems in physics and other sciences**. *Phys. Rev. Lett.*, **96**:188701, May 2006. 51
- [219] H. RATINEY, M. SDIKA, Y. COENRADIE, S. CAVASSILA, D. VAN ORMONDT, AND D. GRAVERON-DEMILLY. **Time-domain semi-parametric estimation based on a metabolite basis set**. *NMR Biomed*, **18**(1):1–13, Feb 2005. 51
- [220] L. VANHAMME, A. VAN DEN BOOGAART, AND S. VAN HUFFEL. **Improved method for accurate and efficient quantification of MRS data with use of prior knowledge**. *J. Magn. Reson.*, **129**:35–45, 1997. 51
- [221] T.F. COLEMAN AND Y. LI. **An interior trust region approach for nonlinear minimization subject to bounds**. Technical report, Cornell University, 1993. 51
- [222] S. W. PROVENCHER. **Estimation of metabolite concentrations from localized in vivo proton NMR spectra**. *Magn Reson Med*, **30**(6):672–679, Dec 1993. 51
- [223] R.R. COIFMAN AND M.V. WICKERHAUSER. **Entropy-based algorithms for best basis selection**. *Information Theory, IEEE Transactions on*, **38**(2):713–718, 1992. 51

Declaration

I herewith declare that I have produced this paper without the prohibited assistance of third parties and without making use of aids other than those specified; notions taken over directly or indirectly from other sources have been identified as such. This paper has not previously been presented in identical or similar form to any other German or foreign examination board.

The thesis work was conducted from XXX to YYY under the supervision of PI at ZZZ.

CITY,